https://doi.org/10.5194/egusphere-2026-2772
Preprint. Discussion started: 27 May 2026

Solid-particle stratospheric aerosol injection: a 2-D modeling exploration of the design space

Yoav Lederer[1], Nahliel Wygoda[1], Dorri Halbertal[1], and Brian E. J. Rose[2]

[1]Stardust Labs, Ness Ziona, Israel
[2]University at Albany, State University of New York, Albany, New York, USA

Correspondence: Yoav Lederer (y.lederer@stardust-initiative.com)

Abstract. Solid-particle alternatives to sulfate for stratospheric aerosol injection (SAI) span a broad parameter space: particle composition and morphology, sensitivities to agglomerate microphysics, and injection strategies in latitude, altitude, and season. Spanning this space with three-dimensional chemistry–climate models is practically prohibitive. To enable such sweeps, we present a two-dimensional (2-D) zonal-mean modeling framework for SAI with solid-particle materials. ERA5-constrained stratospheric transport is coupled with explicit aerosol microphysics and a modified RRTMG radiative transfer scheme, with each component extensively validated. Focusing on silica and calcite, we use the framework to explore SAI performance across two complementary axes: material properties together with monomer and agglomerate microphysics, and injection strategies in space and time. Tropical injection maximizes radiative forcing efficacy but pays the largest in-layer heating penalty. Coagulation in the tropical confinement amplifies aggregate diameters and partially offsets the residence-time advantage. A seasonal schedule (alternating-summer-hemisphere) delivers a modest $\sim$ 10–20% mid-latitude gain in radiative forcing efficacy over symmetric injection, but at a comparable mid-latitude heating-cost penalty. For IR-absorbing materials such as silica, symmetric mid-latitude injection reduces stratospheric heating with limited loss of efficacy; calcite's negligible IR absorption keeps the heating penalty an order of magnitude lower across all injection strategies considered.

1 Introduction

Stratospheric aerosol injection (SAI) has emerged as a potentially viable approach to solar radiation management (SRM), aiming to partially offset the radiative forcing of accumulating greenhouse gasses by deliberately increasing the stratospheric aerosol loading (Budyko, 1977; Teller et al., 1997; Crutzen, 2006). To date, the overwhelming majority of atmospheric modeling studies of SAI have focused on aqueous sulfuric acid aerosols, which serve as the standard reference material for the field (Rasch et al., 2008; Niemeier and Timmreck, 2015; Kleinschmitt et al., 2018; Tilmes et al., 2018; Dai et al., 2018; Visioni et al., 2021, 2023; Bednarz et al., 2023b). There are several physics-side limitations of sulfate-based SAI: decreasing radiative efficiency at higher injection rates due to particle growth and coagulation (Heckendorn et al., 2009; English et al., 2012), lower-stratospheric heating from infrared absorption, and interactions with stratospheric ozone chemistry (Bednarz et al., 2023a). Quantifying these limitations and the climate-system response to candidate SAI strategies remains a central modeling challenge (Eastham et al., 2025).

https://doi.org/10.5194/egusphere-2026-2772
Preprint. Discussion started: 27 May 2026

These limitations have motivated exploration of solid aerosol alternatives. Weisenstein et al. (2015) and Dykema et al. (2016) demonstrated that solid particles could offer advantages including reduced stratospheric heating, improved scattering properties, and the potential for larger achievable radiative forcings. Subsequent work has further developed solid-particle alternatives, both their fundamental optical properties and their representation in coupled chemistry–climate microphysics schemes (Vattioni et al., 2023, 2024), while highlighting that substantial uncertainties remain regarding their full climatic impact (Vattioni et al., 2025).

In the present work, we focus specifically on engineered amorphous silica (SiO_2) and calcite ($CaCO_3$) as candidate materials for SAI (Spector et al., 2026). Engineered amorphous silica particles are attractive because of their chemical inertness in the stratosphere, high refractive index, abundance, bio-compatibility, and extensive industrial experience with large scale manufacturing capabilities. Calcite, while chemically reactive in its bare form, has attracted growing interest in coated configurations. The principal advantage of calcite is its minimal absorption in the longwave infrared, resulting in significantly reduced stratospheric heating compared to sulfate or absorbent solid aerosols (Keith et al., 2016). These two materials are at the center of an engineered sub-micron particle design program (Spector et al., 2026), grounded in a parallel proposal of explicit safety and controllability requirements for any deployed SAI system (Waxman et al., 2026).

Any solid aerosol injected into the stratosphere undergoes coagulation (the collisional sticking of suspended monomers), producing fractal aggregates whose settling velocities, optical properties, and atmospheric lifetimes differ markedly from those of the injected monomers. The coagulation rate scales as the square of the number concentration, so it is strongly enhanced in the tropical pipe where the injected mass concentrates. Sedimentation preferentially removes heavier aggregates, while coagulation continuously generates new ones; the steady-state size distribution reflects this competition. The interplay between injection strategy, particle microphysics, and stratospheric transport creates feedbacks that determine both the efficacy and the spatial distribution of the resulting radiative forcing. The design space that must be swept is broad: particle composition and refractive properties, monomer size and aggregate morphology, the sensitivity of forcing efficacy and stratospheric lifetime to coagulation physics, and injection strategy in latitude, altitude, and season. Spanning this space with three-dimensional chemistry–climate models is practically prohibitive. Stratospheric 2-D models suitable for such surveys already exist, notably the AER 2-D model (Weisenstein et al., 2015) and the NASA Goddard Space Flight Center (GSFC) 2-D model (Fleming et al., 1999). Neither has been used for an SAI parameter survey in the scope undertaken here.

We have developed a zonally averaged two-dimensional (2-D) climate model that couples ERA5-constrained stratospheric transport with explicit aerosol microphysics (coagulation, sedimentation) and a modified RRTMG radiation scheme. The 2-D framework is justified by the rapid zonal mixing of the stratosphere on seasonal and longer timescales, which makes latitude–pressure the natural coordinate system for studying the Brewer–Dobson circulation and its interaction with injected aerosols. The approach bridges simple box models and computationally expensive 3-D Earth System Models, enabling rapid exploration of the parameter space spanned by injection latitude, injection altitude, particle material, and particle morphology.

The transport model is validated against Age of Air measurements, showing fidelity comparable to 3-D Lagranto trajectory calculations, and against the GSFC 2-D model's meridional diffusion coefficient. The microphysics coagulation scheme is benchmarked against the AER 2-D model. The modified RRTMG radiation scheme is validated against MODTRAN (Berk

https://doi.org/10.5194/egusphere-2026-2772
Preprint. Discussion started: 27 May 2026

et al., 2014) calculations with 64-moment scattering. We then apply the model to investigate the sensitivity of SAI performance to injection location, season, and particle properties, demonstrating their interplay.

The remainder of this paper is organized as follows: the model description and validation are presented in Sect. 2, results for base distribution functions, stratospheric dynamics, and forcing efficacy in Sect. 3, and conclusions in Sect. 4.

2 Model description

The framework computes, for each prescribed stratospheric aerosol injection scenario, the steady-state aerosol distribution and its top-of-atmosphere shortwave and longwave radiative response. Three coupled processes are resolved: stratospheric transport by the ERA5-derived residual circulation and eddy diffusion tensor (Sect. 2.1); aerosol microphysics, with explicit coagulation and sedimentation of fractal aggregates (Sect. 2.2); and radiative transfer through a modified RRTMG scheme (Sect. 2.3) that delivers stratosphere-adjusted radiative forcing (SARF) under prescribed tropospheric conditions.

Background fields are taken from the 2008–2017 ERA5 reanalysis (Soci et al., 2024): wind and eddy fields used to derive transport coefficients; ozone and water-vapor mass mixing ratios for the radiation scheme; surface albedo and tropospheric temperature/humidity to anchor the SARF calculation. Other trace gasses (CO_2, N_2O, CH_4, O_2) use current well-mixed values. Integration uses the Climlab Python toolkit (Rose, 2018).

Several feedbacks are deliberately omitted: aerosol radiative heating does not feed back into the transport circulation or eddy diffusion; stratospheric water vapor does not respond to tropopause warming; the lower-boundary loss is a prescribed-tropopause sink rather than a wet-deposition scheme; and ozone chemistry is not coupled to the aerosol surface area. The coagulation kernel assumes a sticking coefficient of unity. Interaction between the injected solid aerosol and the ambient sulfate background is not modeled, since its rate depends on the surface properties of the coated particles. Those simplifications can be relaxed in future work. Surface-temperature are estimated only by an assumed climate sensitivity (Eq. 3); a process-based 2-D climate-response calculation is planned for future work (Sect. 4.3). These choices isolate the transport, microphysics, and direct-radiation response that is the focus of the parameter survey reported here.

2.1 Stratospheric transport

We employ a zonally averaged 2-D model for stratospheric transport, which includes mean advective transport and eddy diffusion. The effects of steady, conservative eddies are represented using the Transformed Eulerian Mean (TEM) formalism (Dunkerton, 1978; Holton, 1981), while transient eddy motions are parameterized as a diffusive flux (Holton, 1981; Pitari and Visconti, 1985). In this framework, the transport equations take an advective–diffusive form. Advection–diffusion parameters are derived from the ERA5 reanalysis over the ten-year period 2008–2017 using Holton's formalism (Holton, 1981). Further details on the derivation of the advection and diffusion coefficients are given in Appendix A.

The transport model was validated against age-of-air (AoA) measurements, which provide information on the mean transport of gasses in the stratosphere (see, e.g., Waugh and Hall, 2002). In an AoA simulation, the tracer concentration under the tropopause is set as proportional to the simulation time, and the mean stratospheric age is defined as the steady-state difference

https://doi.org/10.5194/egusphere-2026-2772
Preprint. Discussion started: 27 May 2026

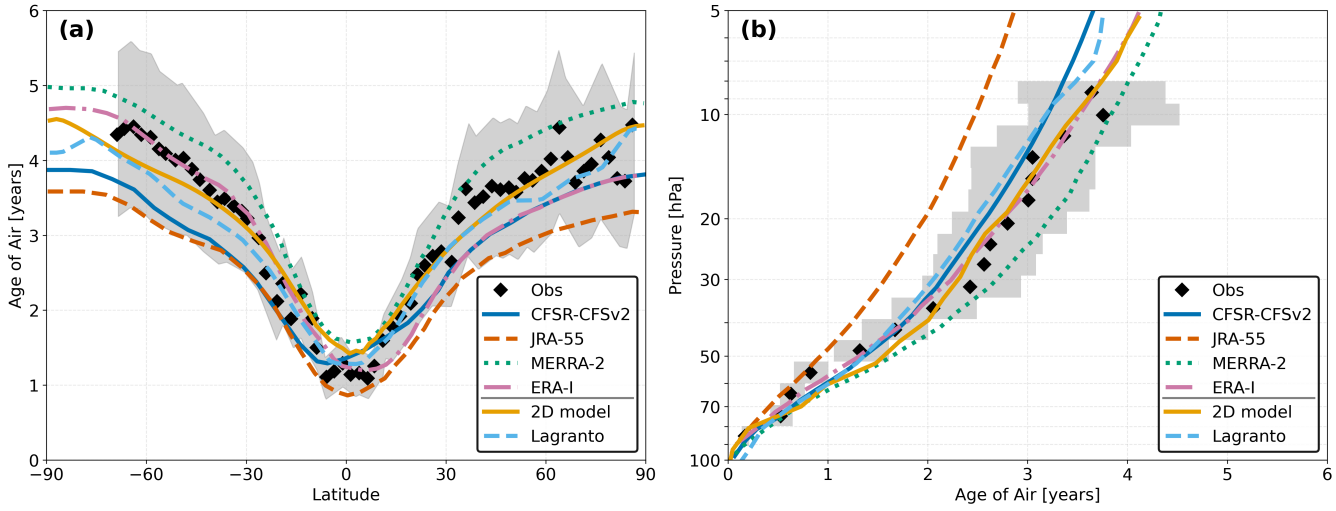

Figure 1. Validation of the 2-D transport model against age-of-air (AoA) measurements. (a) Mean AoA at ~ 50 hPa as a function of latitude. (b) AoA in the deep tropics as a function of pressure. Our 2-D model (orange) and the Lagranto 3-D trajectory calculation (dashed cyan) are overlaid on figure 4 digitized from Chabrillat et al. (2018), showing the multi-reanalysis comparison and CO_2/SF_6 observations. The 2-D model agrees well with both the observations and the Lagranto trajectories, validating the residual-mean transport and eddy mixing.

between the tracer concentration and the current tropospheric value. The simulated AoA is compared both to the values inferred from CO_2 and SF_6 measurements (Waugh and Hall, 2002, and references therein) and to AoA values obtained from a 3-D Lagranto trajectory calculation, as well as to AoA values produced by several reanalyses (Chabrillat et al., 2018). For the validation runs presented in this section the simulations use as input the yearly mean values for the stream function and the diffusion coefficients; the seasonally varying fields are used in all subsequent SAI simulations. The Lagranto (Sprenger and Wernli, 2015) AoA simulations were run using the same 2008-17 ERA5 winds as the 2D simulations. Age of air is calculated in a method similar to Eluszkiewicz et al. (2000), by forward following trajectories injected every 10 days at 95 hPa and at random locations within the latitude range 10S-10N and all longitudes, then averaging the trajectory ages in fixed Eulerian boxes in the stratosphere.

Figure 1 shows the AoA from our 2-D model alongside CO_2/SF_6 observations, the Lagranto 3-D trajectory calculation, and several reanalyses. Panel (a) shows the AoA at ~ 50 hPa as a function of latitude; panel (b) shows the AoA in the deep tropics as a function of pressure. The 2-D model (orange) reproduces the AoA observations, and agrees closely with the Lagranto 3-D trajectory calculation, validating the residual-mean transport and eddy mixing.

2.2 Aerosol microphysics

The model includes explicit coagulation and sedimentation schemes following the formulations in Seinfeld and Pandis (2016). Integration of all physical processes is handled by Climlab (Rose, 2018). This formulation is appropriate for stratospheric

https://doi.org/10.5194/egusphere-2026-2772
Preprint. Discussion started: 27 May 2026

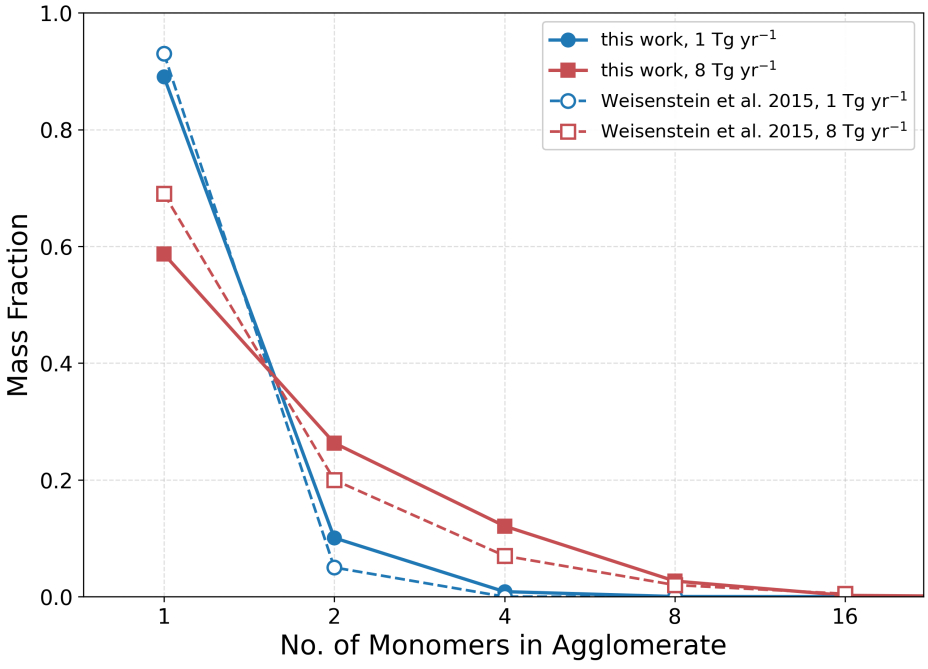

Figure 2. Comparison of the aerosol microphysics module against the AER-2D model. Mass fraction of agglomerates as a function of the number of monomers per agglomerate, for $r_0 = 240$ nm and injection rates of 1 Tg yr^{-1} (blue) and 8 Tg yr^{-1} (red); solid lines show our model results and dashed lines are reference values read from Fig. 4c of Weisenstein et al. (2015). The close agreement validates the microphysics scheme of our 2-D code against this established benchmark.

conditions. In the troposphere, aerosol residence time is assumed negligible; for simplicity, we impose an efficient removal (sink) at the tropopause. A more realistic tropospheric loss scheme can be implemented if needed.

The aerosol microphysics module was benchmarked against the AER-2D model (Weisenstein et al., 2015), which has been extensively used for stratospheric aerosol studies. Figure 2 shows a comparison of the aerosol microphysics module against the AER-2D model: the mass fraction of agglomerates as a function of the number of monomers per agglomerate, for an initial particle radius of $r_0 = 240$ nm and injection rates of 1 and 8 Tg yr^{-1}. Our model (solid lines) captures the equilibrium distribution of mass across particle size bins as computed by the AER-2D model (dashed lines, digitized from Fig. 4c of Weisenstein et al., 2015). The close agreement validates the microphysics scheme of our 2-D code against this established benchmark.

2.3 Radiation

The code implements the RRTMG radiation scheme (see Mlawer et al., 1997; Clough et al., 2005; Oreopoulos et al., 2012 and references therein). Most greenhouse gasses (CO_2, N_2O, O_2 and CH_4) for radiation calculations are assumed to be well mixed

https://doi.org/10.5194/egusphere-2026-2772
Preprint. Discussion started: 27 May 2026

in the atmosphere, with their concentration levels taken to match their current estimated values. The spatial and temporal mass mixing ratios of ozone and water vapor are taken from the monthly ERA5 database.

The monthly mean surface albedo values are calculated using the ERA5 database. The daily averaged insolation latitudinal and temporal dependence is calculated from the instantaneous solar flux, the latitudinal dependence of the zenith and declination angles, and integrating over the daily hour angle (Hartmann, 2016).

Mie scattering calculations are performed for aerosol particle properties. For a given particle's real and imaginary refractive index, parameters such as optical depth, absorption efficiency, scattering, and backscattering efficiencies are calculated as a function of the radius of the particle, incident beam wavelength, and scattering angle. The resulting Mie efficiencies for silica and calcite are reported in Appendix B5. For implementation in RRTMG, it is found that, for typical cases of aerosols with large back scattering, modifications to the code are needed for accurate zonal mean, daily averaged quantities. These modifications follow Coakley and Chylek (1975) and Wiscombe and Grams (1976): in brief, we replace the shortwave reflection and transmission of each aerosol-containing layer in RRTMG with values computed from an explicit Mie-based layer calculation, restoring the accuracy that the unmodified scheme loses for strongly backscattering aerosols. The longwave channel is treated by the unmodified RRTMG, a choice that is physically justified for the particle sizes considered here. The full derivation is described in Appendix B. Furthermore, the cosine of the zenith angle, used in the 2D has to be chosen with care for a consistent diurnal radiative balance (see Appendix B2).

Figure 3 shows the validation of the short wave radiative transfer treatment of the zonally-averaged 2D code against the reference (Solid black lines): a detailed radiative-transfer by MODTRAN (Berk et al., 2014). The test case is a 10 Tg silica layer of silica layer of 0.5 μm-diameter particles, uniformly distributed in $p \in [23, 83]$ hPa (corresponding to $\sim$ 18–22 km), with silica optical properties derived from published data via Mie calculations (see Appendix B5). The background atmosphere is the annual-zonal mean of the reference run of this work, under clear-sky conditions. The solid blue lines in Fig. 3 correspond to a diurnal average of hourly calculations, labeled 3D, as they emulate GCM usage of radiative-transfer calculations. In contrast, the dashed lines, show the result of a single RRTMG call per latitude, emulating 2D code radiative-transfer calculations (blue curve for original RRTMG code, and red curve for the modified RRTMG code presented here). The contrast between the 2D and 3D curves (dashed and solid blue) of the original RRTMG highlight the need for the introduced code modification. Furthermore, the modified RRTMG approach doesn't suffer from the over-estimation of the radiative effect at midlatitudes as the original RRTMG (dashed red vs. blue curves), confirming that the code modification correctly translates the averaging-consistent layer-model coefficients into the two-stream calculation. A residual bias remains in the modified RRTMG: it is much smaller than the original-2D bias and of the same order as the difference between the original 3D RRTMG and MODTRAN. It reflects the intrinsic non-linearity of the back-scattering fraction with respect to the solar zenith angle: no single daily-mean effective zenith-angle cosine can exactly reproduce the diurnally-integrated scattering response.

Finally, since particle coagulation in the stratosphere produces aggregate structures, the validity of using Mie theory for non-spherical particles must be assessed. Discrete Dipole Approximation (DDA) simulations (Yurkin and Hoekstra, 2007) comparing the scattering properties of fractal aggregates to those of volume-equivalent spheres indicate that treating aggregates as effective spheres introduces only minimal overestimation of solar spectrum-weighted backscattering efficiency (see

https://doi.org/10.5194/egusphere-2026-2772
Preprint. Discussion started: 27 May 2026

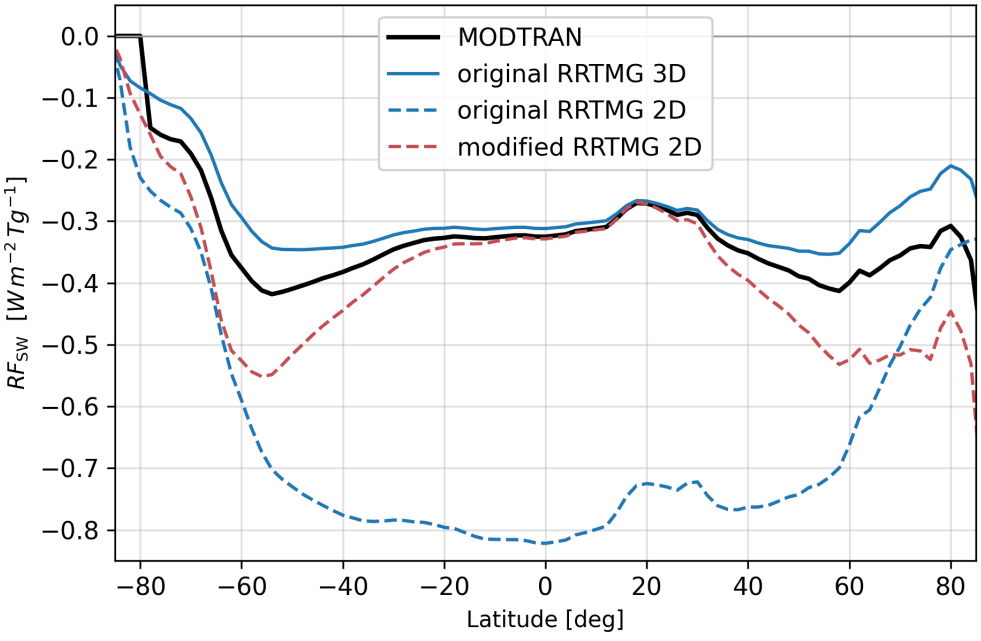

Figure 3. Validation of radiative transfer treatment of the zonally-averaged 2D code. SW radiative forcing per unit burden as a function of latitude for for day-of-year 91 (close to the spring equinox), for a 10 Tg silica layer of 0.5 μm-diameter particles uniform in $p \in [23, 83]$ hPa, under clear-sky conditions with an annual-mean background atmosphere. Solid curves - labeled 3D: RRTMG is called at every hour of the day and the result is integrated diurnally, the way RRTMG is driven inside a 3D GCM (black: MODTRAN with a 64-moment phase function, used as reference; blue: original RRTMG). Dashed curves - labeled 2D: a single RRTMG call per latitude with the daily-averaged cosine of the zenith angle as the only solar-geometry input, the way RRTMG is driven by a zonally-averaged 2D transport model (blue: original; red: modified). The modified RRTMG, used in the 2D code, properly captures the time-averaged solar scattering by the thin layer. See Appendix B2 and B3 for details.

Appendix B6 for details). This justifies the use of Mie calculations with an effective volume-equivalent radius as the approximation adopted throughout this work.

2.4 Definitions and default model setup

For each injection scenario the mean particle lifetime is defined as the steady-state global stratospheric burden M_{tot} divided by the injection rate R, $\tau = M_{\mathrm{tot}}/R$. Steady state is taken as the mean over the final twelve monthly time steps of the ten year run. With coagulation active, the model tracks the aerosol mass distribution across a discrete set of aggregate-size bins indexed by the number of primary monomers per particle, $N \in \{1, 2, 4, 8, 16, 32, 64, 128\}$. From this distribution we compute the mass-weighted mean number of monomers per agglomerate, N_{eff}, and report the corresponding effective agglomerate diameter under the mass-equivalent compact-sphere convention, $d_{\mathrm{eff}} = d_0\, N_{\mathrm{eff}}^{1/3}$, where d_0 is the monomer diameter (so d_{eff} is the diameter of a sphere whose total volume equals that of N_{eff} packed monomers); an alternative would be the fractal radius of

https://doi.org/10.5194/egusphere-2026-2772
Preprint. Discussion started: 27 May 2026

gyration, but we adopt the compact-sphere convention throughout. Global values quoted in the text are obtained by averaging N_{eff} over the simulated stratospheric distribution with each grid cell weighted by its aerosol mass, before applying the same compact-sphere formula. Unless otherwise stated, all results in this section use silica monomers of diameter $d_0 = 0.5$ μm and, where coagulation is active, a fractal aggregate dimension of $D_f = 1.6$ (the chain-like, low-cross-section limit; see Weisenstein et al. (2015) (Eq. 1) for the definition of D_f), and an injection rate of 20 $\mathrm{Tg\ yr^{-1}}$.

We characterize each injection scenario by five steady-state radiative quantities reported throughout Sect. 3. The *Stratospheric-Adjusted Radiative Forcing*, SARF ($\mathrm{W\,m^{-2}}$), is the global-mean top-of-atmosphere net radiative anomaly computed by the modified RRTMG (Sect. 2.3; see Appendix B7 for calculation details). The shortwave contribution to SARF (a negative absorbed-shortwave-radiation, ASR, anomaly) is due to sunlight scattered back to space by the aerosol layer; the longwave contribution (a reduction in outgoing longwave radiation, OLR) is due to absorption and emission of longwave radiation inside the layer, which also drives the stratospheric heating. SARF is a practical upstream proxy for the eventual climate response and for the safety/controllability metrics against which an SAI deployment would be evaluated (Fuglestvedt et al., 2003; Waxman et al., 2026); whether the design-space conclusions reached here at the SARF level translate to the corresponding surface-temperature, hydrological, and ecosystem-response patterns will be tested by the climate-response coupling described in Sect. 4.3. The *SARF efficacy* ϵ folds SARF against the injection mass rate:

$$\epsilon \equiv \frac{\mathrm{SARF}}{R} \quad (\mathrm{W\,m^{-2}\ per\ Tg\ yr^{-1}}), \tag{1}$$

giving the per-unit-mass cooling delivered by a given injection scheme; more-negative ϵ is more design-favorable. We mark the *tropical lower-stratospheric heating peak* by $\Delta T_{\mathrm{peak,trop}}$ (K) (see appendix B7 for calculation details) and then the *heating-cost ratio* η_{heating} that folds heating against cooling:

$$\eta_{\mathrm{heating}} \equiv -\frac{\Delta T_{\mathrm{peak,trop}}}{\mathrm{SARF}} \quad (\mathrm{K\ per\ W\,m^{-2}}), \tag{2}$$

measuring how much in-layer warming is paid per unit radiative cooling delivered, with lower values (more cooling per unit heating). Finally, the *surface-cooling efficacy* $\eta_{T_{\mathrm{surf}}}$ converts the per-rate radiative forcing efficacy ϵ into a predicted surface-temperature response via an estimate of the climate sensitivity of surface temperature to global-mean radiative forcing, $\bar{\lambda}_T$:

$$\eta_{T_{\mathrm{surf}}} \equiv \bar{\lambda}_T \cdot \epsilon \quad (\mathrm{K\ per\ Tg\ yr^{-1}}), \tag{3}$$

with $\bar{\lambda}_T = 0.8\,\lambda_{\mathrm{CO_2}}$, where $\lambda_{\mathrm{CO_2}} \approx 0.76\ \mathrm{K\,(W\,m^{-2})^{-1}}$ is the surface-temperature sensitivity to CO_2 radiative forcing (Forster et al., 2021) and the factor 0.8 accounts for the somewhat smaller surface-temperature response of solar forcings compared to CO_2 forcings of equal magnitude (Modak et al., 2016), giving $\bar{\lambda}_T \approx 0.61\ \mathrm{K\,(W\,m^{-2})^{-1}}$ for SAI-type scenarios.

Equation 3 is a first-order estimate of the global-mean surface-temperature response. It uses a value of $\bar{\lambda}_T$ obtained from CO_2 and uniform solar-forcing sensitivities rather than from a process-based calculation tailored to a stratospheric aerosol layer and its radiative forcing distribution, and it returns a single surface-temperature number per scenario; it does not address the hydrological-cycle response, which is known to differ between greenhouse-gas and SAI forcings even when the

https://doi.org/10.5194/egusphere-2026-2772
Preprint. Discussion started: 27 May 2026

global-mean surface-temperature change is the same (Bala et al., 2008), nor does it capture the meridional and vertical structure of the imposed forcing or the strongly latitude-dependent surface-temperature and precipitation patterns that different SAI injection strategies produce. We therefore treat $\eta_{T_{\mathrm{surf}}}$ throughout as an approximate design metric; quantitatively reliable surface-temperature and hydrological-cycle responses require a coupled, zonal-mean process-based climate-response calculation, planned for future work (Sect. 4.3).

3 Model Results

3.1 Base distribution functions and SAI layer profiles

For SAI simulations, the source injection rate is specified as a function of time and location. A central concept in the analysis of the resulting aerosol layers is the *base distribution function*: for a constant source injection rate at a given latitude and pressure locations, the resulting steady-state aerosol distribution defines the base distribution function for that injection point. Each base distribution function is characterized by a latitudinal column density profile, which is of particular interest because of its direct relationship to the resulting radiative forcing.

As a final validation step for our model, we compare the 2-D model against Lagranto 3-D trajectories (Sprenger and Wernli, 2015), with sedimentation added and without coagulation, for 24 single-point SiO_2 injection scenarios spanning 60°S–60°N and 40, 65, 95, 120 hPa, under identical 2010 ERA5 winds and a common prescribed zonal-mean tropopause sink. Following Sun et al. (2024), we drive the model with ERA5 reanalysis at 3-hourly temporal resolution on a $1^\circ \times 1^\circ$ horizontal grid and 137 vertical model levels. Tracers crossing the tropopause are removed instantaneously. Tropopause heights are taken from ERA5 (Hoffmann and Spang, 2021) and defined, as in Sun et al. (2024), as the lower altitude of the thermal (lapse-rate) and dynamical tropopauses. For consistency with the 2D model, both LAGRANTO and the 2D simulations use the zonal- and monthly-mean tropopause as the removal surface (a temperature-based tropopause is not used, so that any difference between the two simulations reflects stratospheric transport alone). Each comparison run spans five years, with ERA5 winds for 2010 applied cyclically. Every 3 days, 100 tracers are released at a prescribed latitude and pressure with longitudes drawn at random.

Figure 4 shows a comparison of the 2-D transport scheme against Lagranto 3-D trajectories: the ratio $\mathcal{R} = B_{\mathrm{2D}}/B_{\mathrm{Lag}}$ of year-5 global burdens against injection latitude. Figure 5 shows a side-by-side comparison of the base distribution functions from the 2-D model and Lagranto 3-D for three illustrative injection cases, with their corresponding zonal-mean mass mixing ratios and meridional column-density profiles.

As shown, the 2-D model is quantitatively reliable (within $\approx 20\%$) for injections at the higher-altitude grid levels (40 and 65 hPa) at all latitudes and in the tropical and mid-latitude lower stratosphere, and underestimates the global burden by up to $\sim 40\%$ only for extratropical lower-stratospheric injections (case iii of Fig. 5). The shortfall is attributable to the linearization of eddy perturbations built into the residual-circulation closure (Andrews et al., 1987), which breaks down at the polar vortex edge where the eddy field is non-linear due to Rossby wave breaking. This limitation is confined to the coldest, lowest injection altitudes at high latitudes and does not affect the tropical and mid-stratospheric scenarios that dominate the radiatively efficient SAI design space explored below.

https://doi.org/10.5194/egusphere-2026-2772
Preprint. Discussion started: 27 May 2026

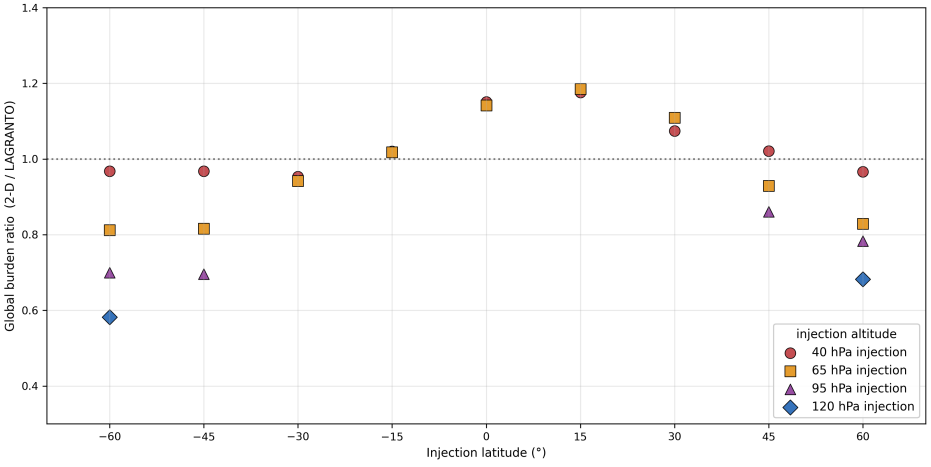

Figure 4. Comparison of the 2-D transport scheme against Lagranto 3-D trajectories. Both include sedimentation. Ratio of global SiO_2 burden (2-D model divided by Lagranto 3-D) for 24 injection scenarios; year-5 average, 2010 ERA5 winds, 0.5 μm particles. The 2-D model agrees with the 3-D benchmark to within $\sim 20\%$ across most of the injection grid, with $\sim 40\%$ shortfalls confined to high-latitude lower-stratospheric injections.

3.2 Stratospheric dynamics and agglomeration physics

We examine three controls on residence time and aggregate size: injection location, fractal dimension, and monomer size.

3.2.1 Role of coagulation and sensitivity to injection location

Figure 6 shows the effect of coagulation on the stratospheric residence time, as a function of injection latitude and pressure: it maps the steady-state mean particle lifetime of 0.5 μm silica particles, with and without coagulation, alongside the global mass-weighted volume-equivalent effective diameter under coagulation, $d_{\mathrm{eff}} = d_0\, N_{\mathrm{eff}}^{1/3}$, where d_0 is the monomer diameter and N_{eff} is the mass-weighted mean number of monomers per agglomerate, so d_{eff} is the diameter of a sphere whose volume equals that of N_{eff} packed monomers (see Sect. 2.4). The 20 $\mathrm{Tg\ yr^{-1}}$ injection rate is chosen such that the coagulation effect is pronounced. The patterns in the three panels expose two competing effects of injection location.

The longest residence times (panels a, b) occur for tropical injections: placing particles in the ascending branch of the Brewer–Dobson circulation lifts them to higher altitudes and forces them through a long meridional transit before they reach the tropopause sink at higher latitudes, and this lengthened circulation path dominates the residence-time budget despite the higher sedimentation velocities encountered at the lower air densities aloft.

The same regime, however, drives the strongest coagulation: the longer residence time and higher particle concentrations in the tropical stratosphere amplify coagulation rates, producing the largest effective diameters in the tropical pipe (panel c). Larger particles settle faster under gravity, so the lifetime gain expected from the favorable circulation is partially offset by faster sedimentation of the resulting aggregates.

https://doi.org/10.5194/egusphere-2026-2772
Preprint. Discussion started: 27 May 2026

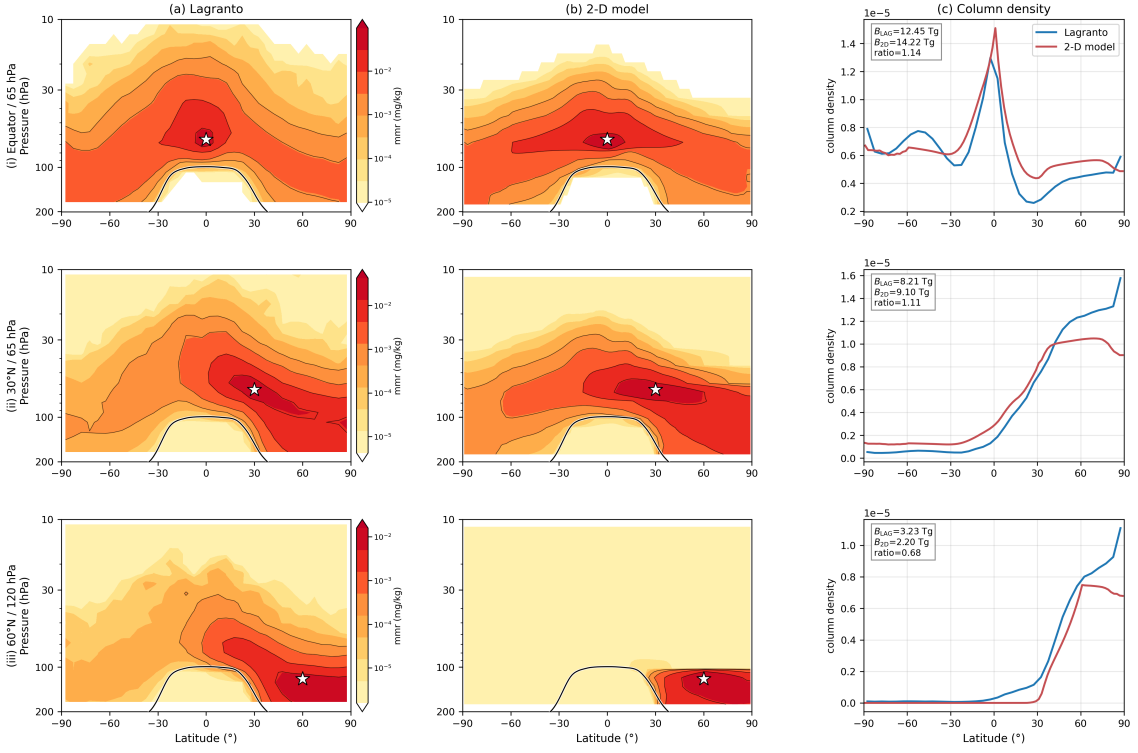

Figure 5. Side-by-side comparison of base distribution functions from the 2-D model and Lagranto 3-D for three illustrative injection cases. Rows: (i) equator / 65 hPa, (ii) 30°N / 65 hPa, (iii) 60°N / 120 hPa. Columns: (a) zonal-mean mass mixing ratio from Lagranto and (b) from the 2-D model (mg kg^{-1}); (c) zonal-mean column density vs. latitude for both models. Black star: injection location; thick black line: 2010 ERA5 zonal-mean tropopause. The 2-D model reproduces the spatial structure and column-density profile of the Lagranto solution in the tropical and mid-latitude cases (i, ii); the high-latitude lower-stratospheric shortfall in case (iii) is attributed to the linearization of eddy perturbations built into the residual-circulation closure (Andrews et al., 1987), which breaks down at the polar vortex edge where the eddy field is non-linear due to Rossby wave breaking.

3.2.2 Role of agglomerate shape

The agglomerate shape, parameterized by the fractal dimension D_f, sets the relationship between an aggregate's mass and its effective cross-section. Loose, chain-like aggregates ($D_f = 1.6$) have a much larger cross-section per unit mass than compact spheres ($D_f = 3.0$), which substantially reduces their sedimentation velocity (see Fig. 1 of Weisenstein et al., 2015). Thus, loose aggregates outlast compact ones by $\sim 10\%$ across most of the injection grid and up to $\sim 40\%$ in the tropical pipe (Fig. 7), with a comparable amplification of the effective aggregate diameter (not shown). A control run with the $D_f = 1.6$ coagulation kernel but $D_f = 3.0$ sedimentation reproduces the $D_f = 3.0$ result almost exactly: the fractal dimension enters the simulation almost entirely through the sedimentation velocity, confirming Weisenstein et al. (2015).

https://doi.org/10.5194/egusphere-2026-2772
Preprint. Discussion started: 27 May 2026

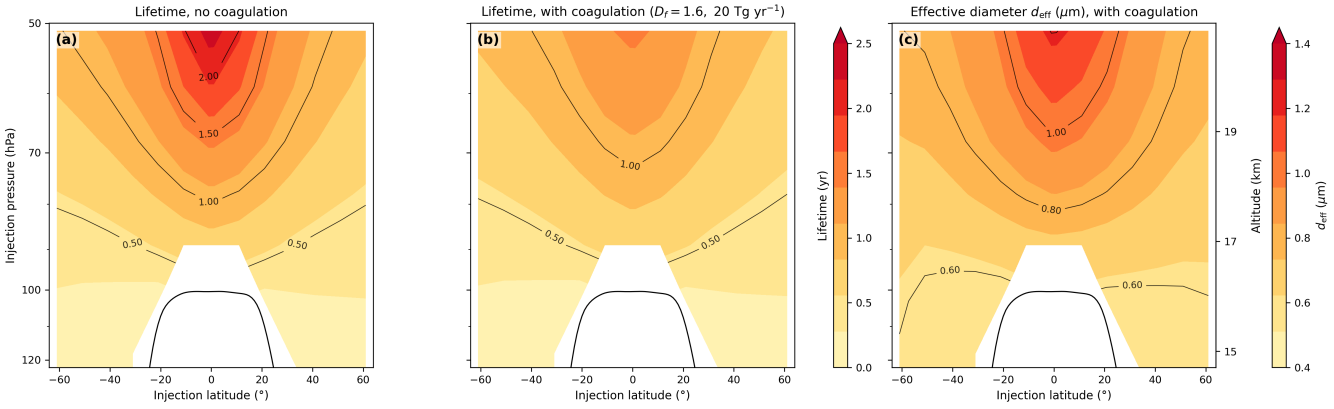

Figure 6. Effect of coagulation on the stratospheric residence time, as a function of injection latitude and pressure. Maps for 20 Tg yr^{-1} injection of 0.5 μm silica particles. (a) Mean particle lifetime (years) without coagulation; (b) Mean particle lifetime (years) with coagulation; (c) global mass-weighted effective diameter (μm) under the same coagulation case. Black contour: annual zonal-mean ERA5 tropopause. Tropical pipe injections give the longest residence times (a, b) by placing particles in the ascending branch of the Brewer–Dobson circulation, but the same regime drives the strongest coagulation and largest effective diameter (c), so the lifetime gain from the favorable circulation is partially offset by faster sedimentation of the larger aggregates.

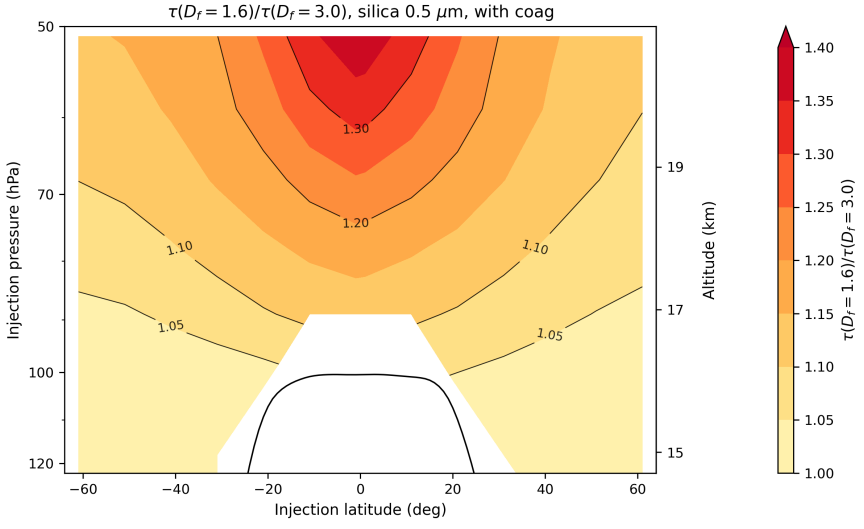

Figure 7. Effect of fractal dimension on the stratospheric residence time, as a function of injection latitude and pressure. Lifetime ratio $\tau(D_f{=}1.6)/\tau(D_f{=}3.0)$ for 0.5 μm silica particles with coagulation at 20 Tg yr^{-1}. Loose aggregates ($D_f{=}1.6$) outlast compact ones ($D_f{=}3.0$) by $\sim 10\%$ across most of the injection grid and up to $\sim 40\%$ in the tropical pipe; the gain is almost entirely a sedimentation effect, with the coagulation kernel itself playing only a marginal role.

https://doi.org/10.5194/egusphere-2026-2772
Preprint. Discussion started: 27 May 2026

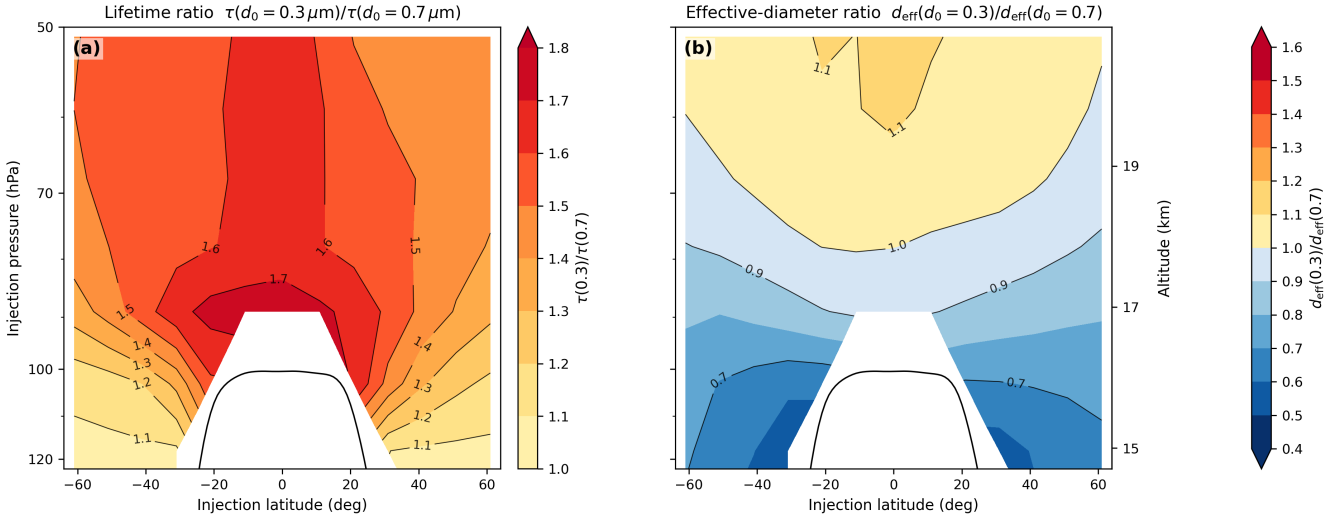

Figure 8. Effect of monomer core diameter on residence time and aggregate size, as a function of injection latitude and pressure. Maps show the ratio between 0.3 μm and 0.7 μm silica particles at 20 Tg yr^{-1} injection. (a) lifetime ratio $\tau(0.3)/\tau(0.7)$; (b) ratio of global mass-weighted effective diameter, $d_{\text{eff}}(0.3)/d_{\text{eff}}(0.7)$. Black contour: annual zonal-mean ERA5 tropopause. Smaller monomers retain a substantial lifetime advantage across the stratosphere (up to $\sim 70\%$, typically $\sim 50\%$; panel a). Despite their smaller starting size, the 0.3 μm particles can aggregate enough to become effectively larger than the 0.7 μm monomers (panel b, values > 1 shown in yellow).

3.2.3 Role of monomer size

Monomer diameter trades two competing effects: smaller monomers have lower mass-specific sedimentation velocity (longer lifetime) but higher number concentration per unit mass (faster coagulation, larger aggregates). Even with coagulation active, the smaller-monomer scenario keeps a substantial lifetime advantage across the stratosphere, up to $\sim 70\%$ and typically $\sim 50\%$ for 0.3 μm versus 0.7 μm monomers (Fig. 8a). The aggregate-size response (panel b) flips sign across the grid: in the tropical pipe the 0.3 μm particles coagulate so heavily that the resulting aggregates exceed those produced from 0.7 μm monomers, while at high latitudes and lower altitudes the larger monomers naturally produce the larger aggregates.

3.3 Radiative forcing and stratospheric heating

We map the radiative forcing efficacy ϵ (Eq. 1) and the heating cost η_{heating} (Eq. 2) across the (latitude, pressure) injection grid for two reference materials: silica (SiO_2, $\rho = 2200\ \text{kg m}^{-3}$) and calcite ($CaCO_3$, $\rho = 2710\ \text{kg m}^{-3}$). For each material we use spectrally-resolved complex refractive indices and compute Mie scattering and absorption coefficients over the RRTMG shortwave and longwave bands (Sect. 2.3, Appendix B); the resulting material-specific Mie efficiencies are tabulated in Appendix B5. Each material is run at its most-efficacious monomer diameter from a sweep of $d_0 \in \{0.3, 0.5, 0.7\}$ μm: silica at $d_0 = 0.5$ μm (the bare-monomer SW Mie peak) and calcite at $d_0 = 0.3$ μm (calcite's Mie peak is located at smaller diameters).

https://doi.org/10.5194/egusphere-2026-2772
Preprint. Discussion started: 27 May 2026

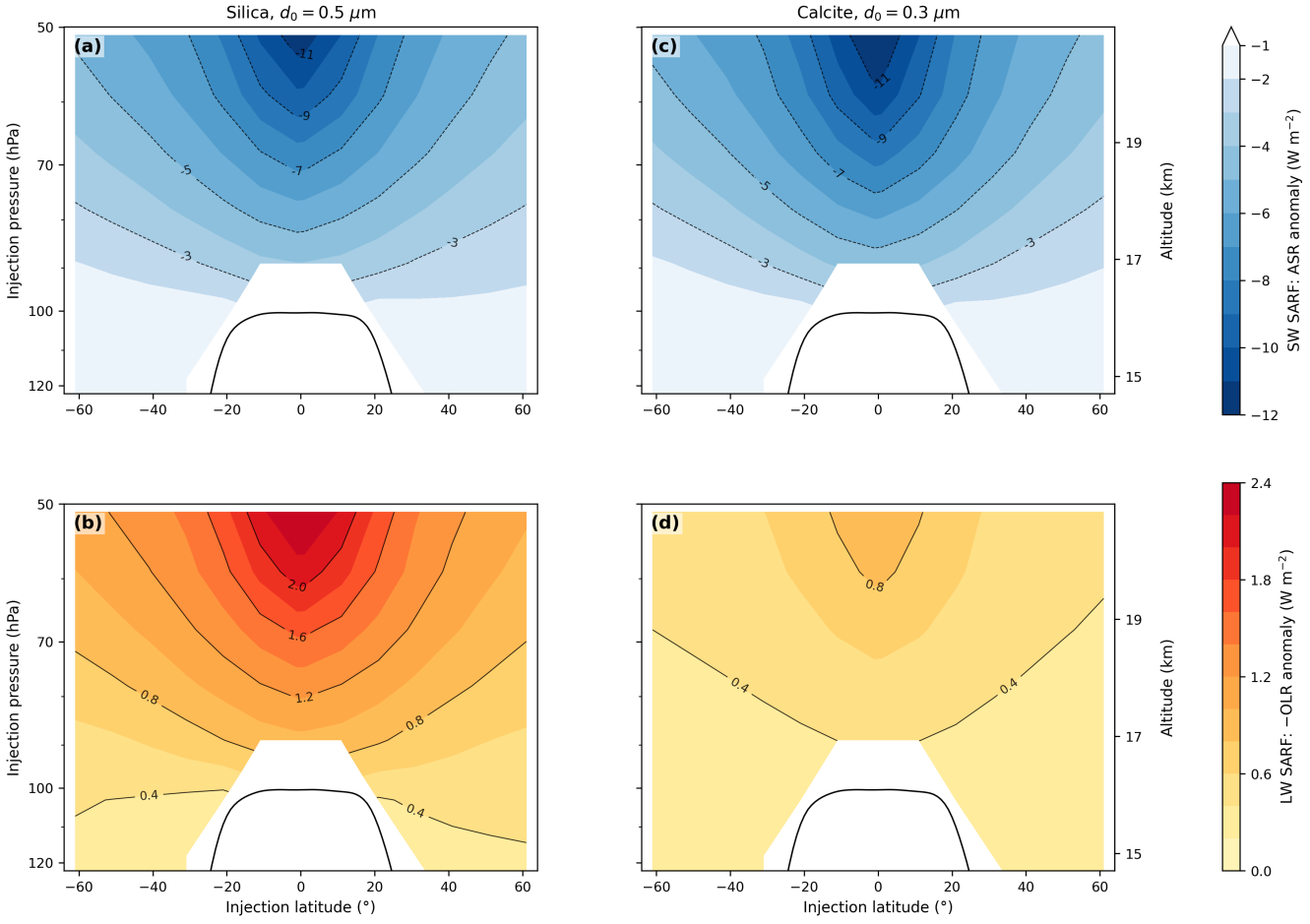

Figure 9. Shortwave (cooling) and longwave (warming) components of the SARF for silica and calcite at 20 $\mathrm{Tg\,yr^{-1}}$, no coagulation, as a function of injection latitude and pressure. Columns: (a, b) silica $d_0 = 0.5$ μm; (c, d) calcite $d_0 = 0.3$ μm. Top row (a, c): SW SARF (ASR anomaly, $\mathrm{W\,m^{-2}}$, negative for cooling). Bottom row (b, d): LW SARF ($-$OLR anomaly, $\mathrm{W\,m^{-2}}$, positive when LW is absorbed in the stratosphere). Black contour: annual zonal-mean ERA5 tropopause.

Figure 9 decomposes the SARF into shortwave and longwave components for silica and calcite, no coagulation. The two materials match in SW (peaking near -12 $\mathrm{W\,m^{-2}}$ in the tropical pipe) but differ by roughly threefold in LW: silica peaks at ~ 2.4 $\mathrm{W\,m^{-2}}$ versus ~ 0.8 $\mathrm{W\,m^{-2}}$ for calcite. The mechanism behind this difference is taken up in Sect. 3.5.

Coagulation modifies the optimal silica monomer choice. Figure 10 shows the SARF ratio $\mathrm{SARF}(d_0 = 0.3)/\mathrm{SARF}(d_0 = 0.5)$ as a function of injection latitude and pressure, both without coagulation (panel a) and with coagulation (panel b). Without coagulation, the ratio remains close to unity across the grid. This is because the longer mean aerosol lifetime of 0.3 μm monomers is offset by their position further from the SW Mie peak relative to 0.5 μm monomers. Under coagulation, the smaller monomer outperforms by 20–60% in the tropical lower stratosphere, because aggregation grows 0.3 μm monomers

https://doi.org/10.5194/egusphere-2026-2772
Preprint. Discussion started: 27 May 2026

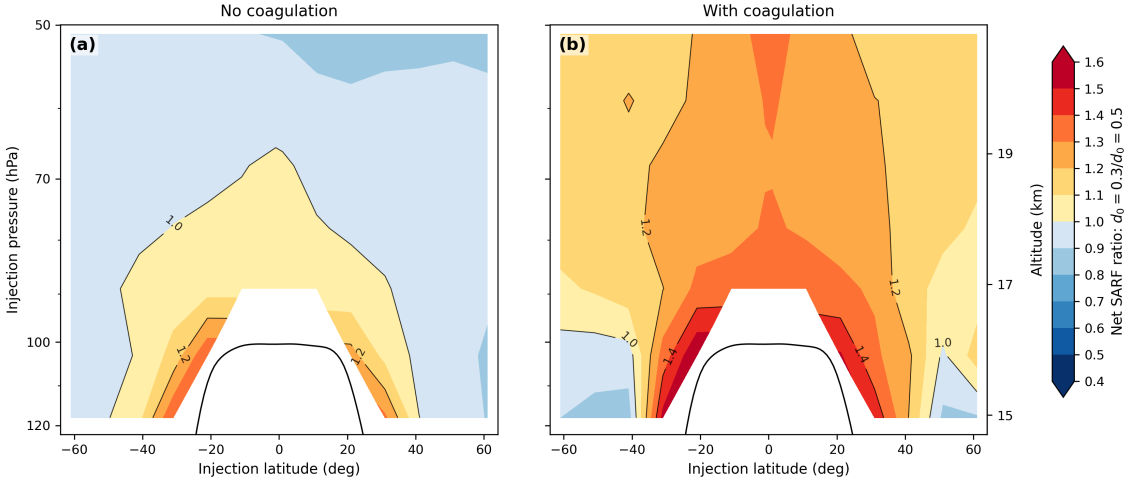

Figure 10. Effect of coagulation on the optimal silica monomer size, as a function of injection latitude and pressure. SARF ratio $\mathrm{SARF}(d_0 = 0.3\ \mu\mathrm{m})/\mathrm{SARF}(d_0 = 0.5\ \mu\mathrm{m})$ at 20 $\mathrm{Tg\ yr^{-1}}$. (a) without coagulation; (b) with coagulation. Black contour: annual zonal-mean ERA5 tropopause. Without coagulation the ratio stays close to unity across the grid since the gain in lifetime approximately compensates for the lower back-scatter efficiency of the 0.5 μm monomers; under coagulation the smaller monomer wins by 20–60% in the tropical lower stratosphere, because aggregation grows 0.3 μm monomers into aggregates of comparable size to those formed by 0.5 μm monomers, placing both at a similar position within the Mie regime, while 0.3 μm monomers retain a substantial advantage in lifetime.

into aggregates of comparable size to those formed by 0.5 μm monomers (as shown in Figure 8 for 0.3 μm vs. 0.7 μm monomers), placing both at a similar position within the Mie regime, while 0.3 μm monomers retain a substantial advantage in lifetime. We use $d_0 = 0.5\ \mu$m as the silica reference in the figures that follow, to keep continuity with the no-coagulation analysis where $d_0 = 0.5\ \mu$m sits at the bare-monomer SW Mie peak.

All subsequent figures use the with-coagulation case. Figure 11 maps ϵ and η_{heating} across the injection grid for silica $d_0 = 0.5\ \mu$m (panels a, c) and calcite $d_0 = 0.3\ \mu$m (panels b, d), both with coagulation, under symmetric (year-round, both-hemispheres) injection (Zhang et al., 2024). The silica panels are discussed here; the calcite panels and the cross-material comparison are taken up in Sect. 3.5. The radiative forcing efficacy (panel a) peaks in the tropical pipe ($|\varphi| < 10°$, 50–80 hPa) at $\epsilon \approx -0.27\ \mathrm{W\,m^{-2}\,(Tg\ yr^{-1})^{-1}}$, where the longest residence time and the largest insolation overhead combine; it drops monotonically poleward and downward, reaching $\epsilon \approx -0.05$ at the high-latitude lower stratosphere. The heating cost (panel c) shows the same tropical pipe paying the largest heating penalty ($\eta_{\mathrm{heating}} \approx 2\ \mathrm{K\,(W\,m^{-2})^{-1}}$); at the mid-latitude lower-strat band (30–50°, 90–110 hPa) η_{heating} is approximately two times smaller, at the cost of ϵ being 2–3 times smaller. The two metrics trade off spatially across the entire grid: the regions that maximise radiative forcing efficacy also maximise the heating cost.

https://doi.org/10.5194/egusphere-2026-2772
Preprint. Discussion started: 27 May 2026

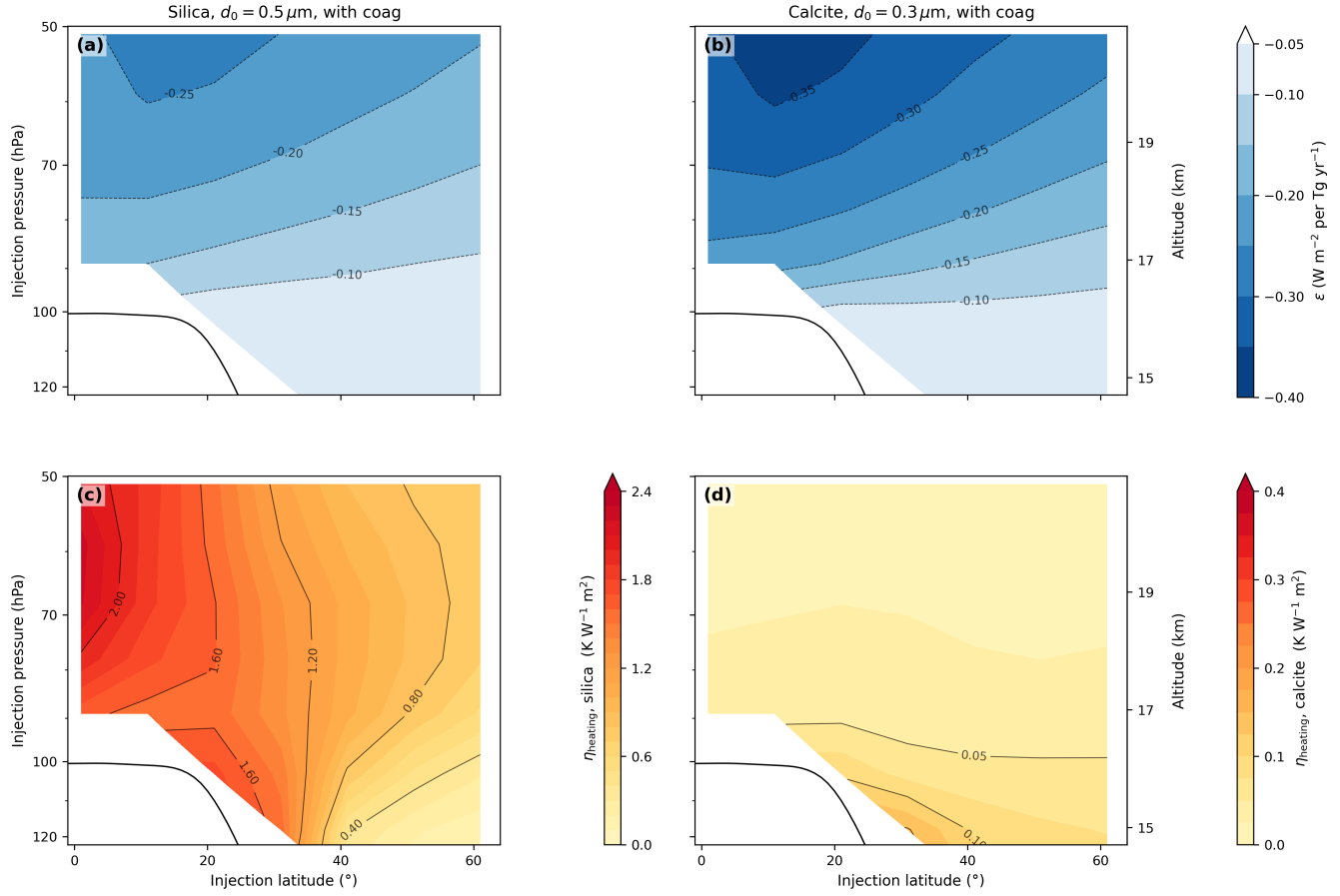

Figure 11. Radiative forcing efficacy (top row, ϵ, W m^{-2} per Tg yr^{-1}; see Eq. 1) and heating cost (bottom row, η_{heating}, K per W m^{-2}; see Eq. 2) of symmetric (year-round, both-hemispheres) injection at 20 Tg yr^{-1} total, as a function of injection latitude and pressure. Columns: (a, c) silica $d_0 = 0.5$ μm with coagulation; (b, d) calcite $d_0 = 0.3$ μm with coagulation. The ϵ panels share a single color scale; the η_{heating} panels use per-material scales reflecting the large difference in heating cost between the two materials (silica color-scale extends to 2.4 and captures the silica field, which peaks near 2.2; the calcite color-scale extends to 0.16 and is deliberately saturated in the high-latitude lower-stratospheric corner where the calcite field reaches ~ 0.36, so the structure over the rest of the grid remains legible). The injection-latitude axis is the NH coordinate of the bilateral injection. Black contour: annual zonal-mean ERA5 tropopause (NH portion). Radiative forcing efficacy peaks in the tropical pipe where the residence time is longest, while the same region pays the largest heating penalty for silica; calcite's heating cost stays an order of magnitude lower than silica's across most of the radiatively-active stratosphere, with the materials approaching parity only at calcite's own peak in the high-latitude lower stratosphere.

3.4 Role of injection season

The symmetric-injection analysis of Sect. 3.3 held the injection rate constant year-round in both hemispheres. Alternatively, a seasonal strategy can be employed in which each hemisphere is injected only during its local spring and summer half-year

https://doi.org/10.5194/egusphere-2026-2772
Preprint. Discussion started: 27 May 2026

(i.e. March through August for the Northern Hemisphere, and September through February for the Southern Hemisphere). We compare the two for the same silica $d_0 = 0.5$ μm, coagulating, 20 $\mathrm{Tg\ yr^{-1}}$ scenario.

Figure 12 shows the radiative forcing efficacy ϵ and heating cost η_{heating} for the seasonal scheme, on the same color scales as Fig. 11 for direct comparison. The tropical pipe ($|\varphi| < 10°$, 50–80 hPa) is schedule-insensitive: ϵ peaks at $\approx -0.27\ \mathrm{W\,m^{-2}\,(Tg\ yr^{-1})^{-1}}$ in both schemes, and $\eta_{\mathrm{heating}} \approx 2\ \mathrm{K\,(W\,m^{-2})^{-1}}$. Outside that core, the seasonal scheme delivers a modest efficacy gain (ϵ improves by ~ 10–20% over much of the mid-latitude lower stratosphere) and the heating penalty extends further from the tropical core into mid-latitudes, with η_{heating} rising by ~ 0.1–$0.4\ \mathrm{K\,(W\,m^{-2})^{-1}}$ across the mid-latitude lower-stratospheric band. Calcite ($d_0 = 0.3$ μm, with coagulation) shows the same ~ 10–20% mid-latitude gain in radiative forcing efficacy and a comparable mid-latitude heating-cost penalty (seasonal-vs-symmetric ratio maps not shown).

The mechanism is the seasonal cycle of the summer-hemisphere lower stratosphere. A seasonal pulse delivers the entire annual mass during the local summer, when the tropopause is at its highest and the descending branch of the Brewer–Dobson circulation is at its weakest, so the local aerosol burden builds to a higher peak than the year-round symmetric baseline; this increases efficacy, but also results in more LW absorption. The relative size of these two effects depends on injection latitude: in the tropical pipe the LW signal is intrinsically small (the column above is thin), so efficacy and heating-cost gains roughly cancel and the schedule effect is weak; in the mid-latitude lower stratosphere the column above is thick, the LW absorption is large, and the heating-cost penalty exceeds the efficacy gain. A test calculation with the NH injection window shifted 3 months earlier (NH injection during winter and spring rather than spring and summer) reduces the radiative forcing efficacy by ~ 10–15%, confirming that the standard seasonal alignment with peak NH-summer overhead insolation is the more favorable choice.

3.5 Implications for SAI strategies

Section 3.3 mapped the silica-only sweep across injection latitude and altitude. We now return to the second design axis, the choice of injection material. Figure 11 makes the $(\epsilon, \eta_{\mathrm{heating}})$ trade-off visible at the cell level for both materials under symmetric injection; the seasonal case (Fig. 12, Table 1) reaches the same material-comparison conclusions. Across the grid the heating cost differs by more than an order of magnitude: silica pays a substantial heating penalty of ~ 0.1–$2.2\ \mathrm{K\,(W\,m^{-2})^{-1}}$, peaking in the tropical pipe where the longest residence time of the absorbing layer combines with the maximum overhead insolation, while calcite sits within 0.0–$0.36\ \mathrm{K\,(W\,m^{-2})^{-1}}$ across the entire grid (calcite's near-Rayleigh LW absorption is weak across the lower-stratospheric column, so in-layer heating per unit |SARF| delivered is negligible). Switching from silica (or sulfate, by extension) to calcite therefore yields a more-than-order-of-magnitude reduction in stratospheric heating per unit |SARF| delivered. The radiative forcing efficacies of the two materials are reported in Table 1; we do not draw a direct quantitative efficacy comparison here, since the silica reference uses $d_0 = 0.5$ μm, which is not the optimal silica diameter under coagulation (Sect. 3.2.3).

The order-of-magnitude difference in heating cost between the two materials is substantially larger than the few-fold difference in their net longwave SARF at the top of the atmosphere (Fig. 9). The driver is the effective source temperature of the longwave radiation each material absorbs, not the absorption coefficients alone. Silica's longwave absorption peaks inside

https://doi.org/10.5194/egusphere-2026-2772
Preprint. Discussion started: 27 May 2026

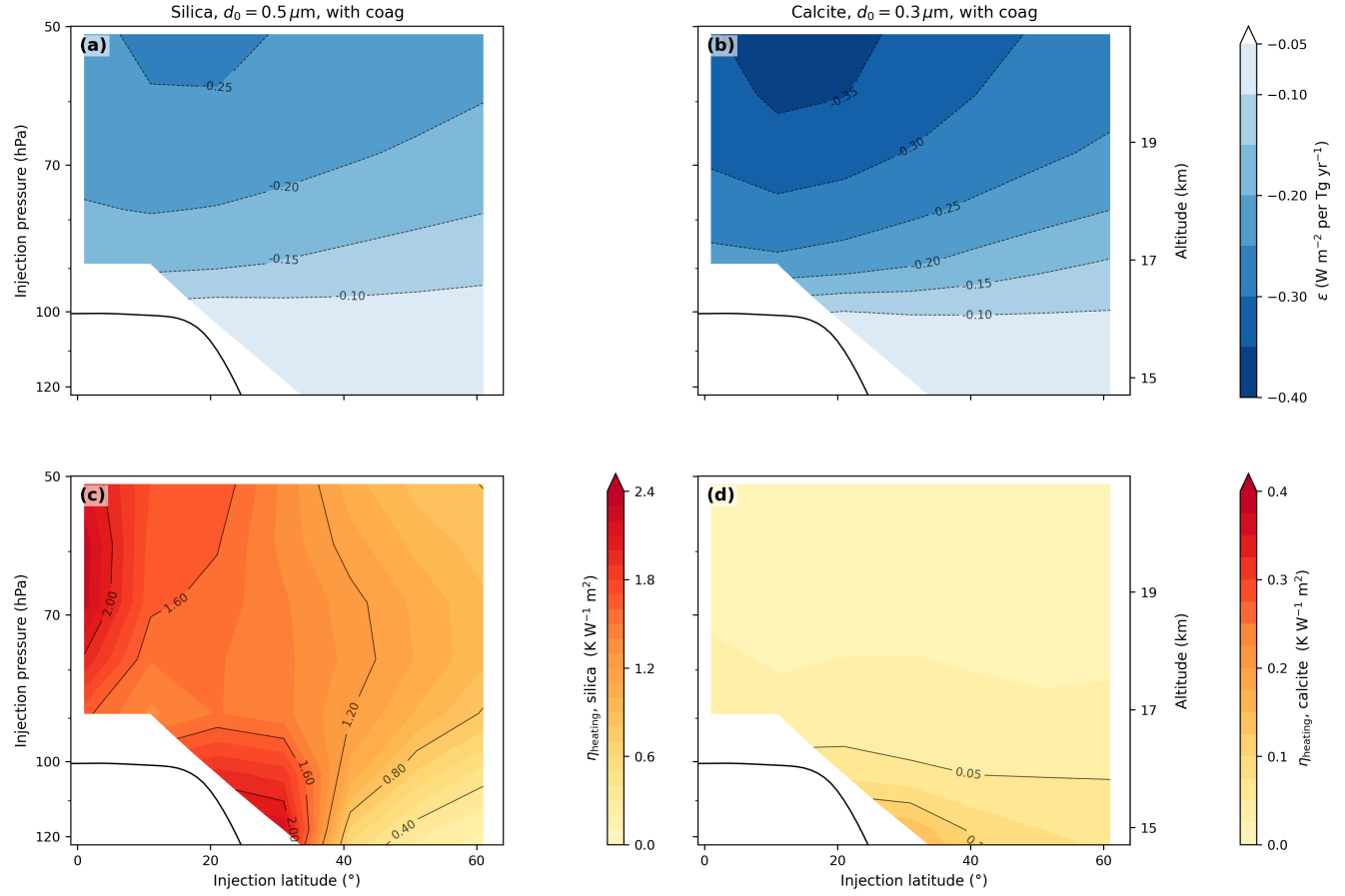

Figure 12. As Fig. 11, but for seasonal (alternating-summer-hemisphere) injection: each hemisphere is injected only during its local summer half-year, with the same total annual rate of 20 Tg yr^{-1}. Same color scales and panel layout (silica panels a, c; calcite panels b, d) as Fig. 11 so the two figures can be compared by eye.

the 8–13 μm atmospheric window, where the upwelling longwave originates almost directly from the warm Earth surface ($\sim$ 290 K); the absorbing layer is driven strongly out of radiative equilibrium with its source and warms substantially. Calcite's longwave absorption sits predominantly outside the atmospheric window, where the column above the surface is already optically thick to thermal radiation, so the photons calcite intercepts originate from neighboring upper-tropospheric and lower-stratospheric layers at temperatures comparable to that of the calcite-laden layer itself.

A tropical injection in the 50–80 hPa layer maximises SARF efficacy for both silica and calcite, due to the longer residence time, while mid-latitude injection at lower altitude (e.g., latitude $\sim 40°, 90\ hpa$) reduces SARF efficacy by $\sim 40\%$ and reduces the heating peak by a comparable factor (it is noted that these injections are operationally easier due to the lower injection altitude). The choice of material has the larger effect: at fixed scenario, calcite reduces the heating cost by more than an order of magnitude compared to silica (and, by extension, sulfate). The result of combining a tropical injection with a calcite

https://doi.org/10.5194/egusphere-2026-2772
Preprint. Discussion started: 27 May 2026

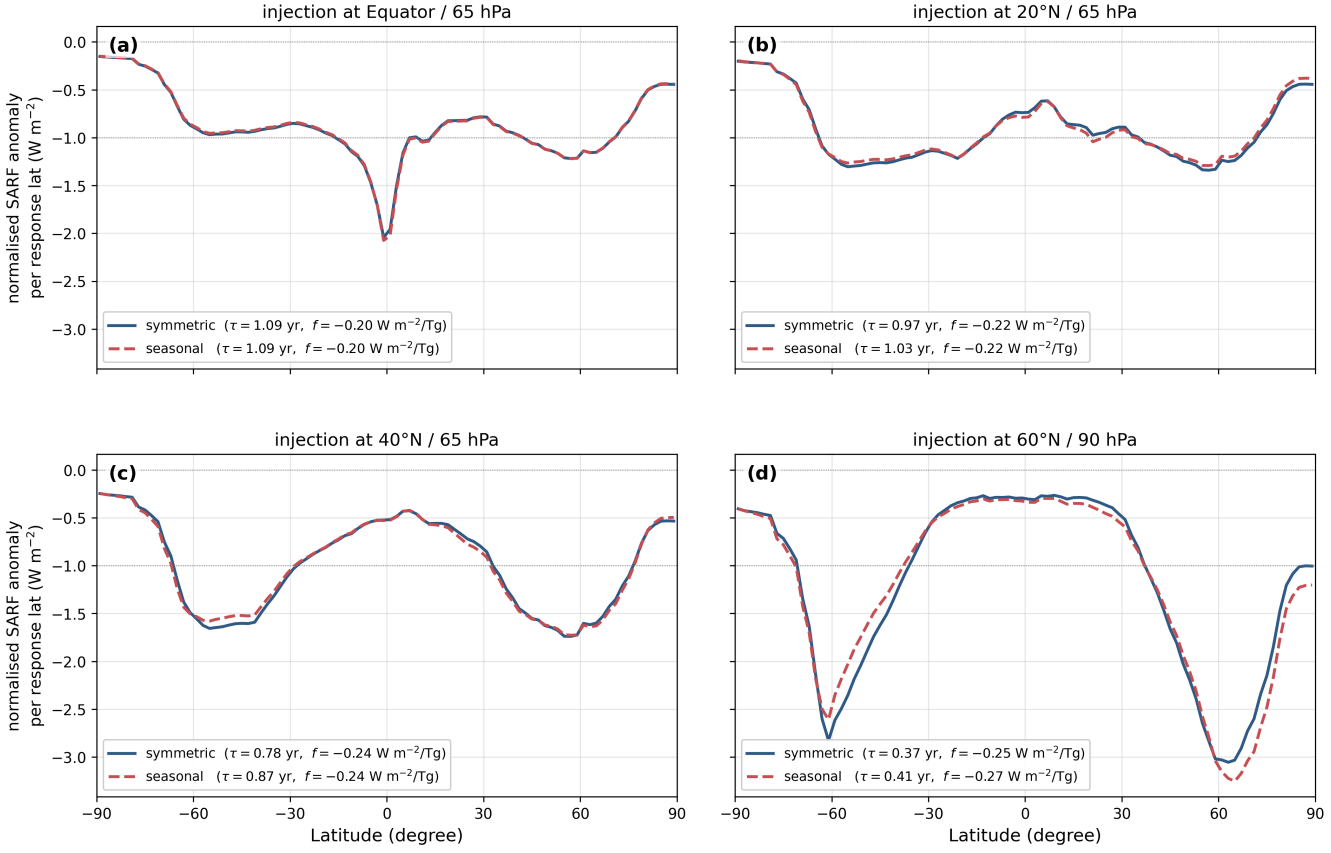

Figure 13. Yearly mean meridional SARF profiles for symmetric (solid blue) and seasonal (dashed red) injection at four representative injection cells (panels a–d: injection at 0°/65 hPa, 20°/65 hPa, 40°/65 hPa, and 60°/90 hPa, respectively), normalized so the global cosine-weighted mean of each curve equals $-1\ \mathrm{W\,m^{-2}}$. Material: silica $d_0 = 0.5\ \mu$m with coagulation at $20\ \mathrm{Tg\ yr^{-1}}$ total. The legend in each panel reports, for each schedule, the stratospheric mean lifetime τ [yr] and the SARF per stratospheric burden $f \equiv \mathrm{SARF}/B$ [$\mathrm{W\,m^{-2}/Tg}$]. The meridional shape of the SARF differs markedly across the four cells: the forcing distribution broadens, narrows, and shifts hemispherically with injection latitude, showing that injection latitude largely sets the meridional RF distribution.

monomer is a near-zero stratospheric heating penalty for typical SARF amplitudes, mitigating the dominant first-order risk of the indirect dynamical and chemical feedbacks that accompany lower-stratospheric warming (Keith et al., 2016). Table 1 reports illustrative values of τ, ϵ, η_{heating}, and $\eta_{T_{\mathrm{surf}}}$ for silica ($d_0 = 0.5\ \mu$m) and calcite ($d_0 = 0.3\ \mu$m), both with coagulation, under seasonal injection at two cells (tropical, 0°/65 hPa ≈ 18.5 km; midlatitude, 45°/90 hPa ≈ 17 km). The silica entries use $d_0 = 0.5\ \mu$m for continuity with the no-coagulation analysis (Sect. 3.2.3) and are not the silica optimum under coagulation, so $|\epsilon|$ for silica should be read as conservative; the values are illustrative and preliminary. For context, the GLENS sulfate-feedback ensemble reports a surface-cooling efficacy of $\sim -0.10\ \mathrm{K\,(Tg(SO_2)\,yr^{-1})^{-1}}$ (Tilmes et al., 2018), comparable on a per-Tg-injected-mass basis to the silica tropical value here (-0.13). The similarity is due to the fact that sulfate has optical properties

https://doi.org/10.5194/egusphere-2026-2772
Preprint. Discussion started: 27 May 2026

Table 1. Illustrative numbers. Performance metrics for silica ($d_0 = 0.5$ μm) and calcite ($d_0 = 0.3$ μm), both with coagulation, under seasonal (alternating-summer-hemisphere) injection at 20 $\mathrm{Tg\ yr^{-1}}$ total, evaluated at two representative single-cell injection scenarios: *tropical* (0°, 65 hPa ≈ 18.5 km) and *midlatitude* (45°, 90 hPa ≈ 17 km). Columns: τ, the aerosol mean particle lifetime (steady-state burden divided by injection rate); ϵ, the radiative forcing efficacy (Eq. 1); η_{heating}, the heating cost (Eq. 2); $\eta_{T_{\mathrm{surf}}}$, the surface-cooling efficacy (Eq. 3). Values are interpolated from the discrete (latitude, pressure) injection grid; they are intended only as an illustration of the design trade-off and not yet appropriate for quantitative use.

Material	Scenario	τ [yr]	ϵ [$\mathrm{W\,m^{-2}\,(Tg\ yr^{-1})^{-1}}$]	η_{heating}[a] [$\mathrm{K\,(W\,m^{-2})^{-1}}$]	$\eta_{T_{\mathrm{surf}}}$ [$\mathrm{K\,(Tg\ yr^{-1})^{-1}}$]
SiO_2, $d_0 = 0.5$ μm	Tropical	1.15	−0.22	2.31	−0.13
(with coagulation)	Midlatitude	0.47	−0.13	1.11	−0.08
$CaCO_3$, $d_0 = 0.3$ μm	Tropical	1.31	−0.31	0.02	−0.19
(with coagulation)	Midlatitude	0.55	−0.17	0.03	−0.10

[a] The values do not reflect the response of stratospheric transport to the aerosol-induced diabatic heating, which is not yet coupled in the present framework.

comparable to silica (see Appendix B5). However, sulfate efficacies decline with injection rate through particle growth and saturation (Niemeier and Timmreck, 2015; Kleinschmitt et al., 2018), an effect that the present coagulation microphysics resolves explicitly for solid particles.

Finally, beyond global radiative forcing efficacy and heating cost, injection latitude also sets the meridional shape of the SARF. This is demonstrated in Fig. 13, which shows the yearly mean meridional SARF profiles for symmetric (solid blue) and seasonal (dashed red) injection at four representative injection cells: the forcing distribution broadens, narrows, and shifts hemispherically with injection latitude, providing a degree of freedom over the meridional RF profile that can address the hemispheric-asymmetry requirements of safety- and controllability-driven SAI design (Waxman et al., 2026). The pattern-effect consequences of this RF shape on surface temperature and the hydrological cycle, which determine whether this latitudinal flexibility translates into a comparable degree of freedom in the climate response, will be studied in future work (Sect. 4.3). Note that the normalized meridional SARF profiles for the symmetric and seasonal cases are nearly indistinguishable.

4 Discussion and outlook

We have developed a computationally efficient two-dimensional (2-D) zonal-mean modeling framework that couples ERA5-constrained stratospheric transport with explicit aerosol microphysics and a modified RRTMG radiation scheme, and have used it to map out the dependence of stratospheric aerosol injection (SAI) performance on injection latitude, injection altitude, and particle properties. The present work deliberately restricts its scope to transport, microphysics, and radiation; stratospheric chemistry and the interaction between the aerosol layer and the large-scale circulation (through radiative heating) are left for future extensions. This permits a quantitative exploration of the design space for solid aerosols, silica and calcite in particular,

https://doi.org/10.5194/egusphere-2026-2772
Preprint. Discussion started: 27 May 2026

at a computational cost that would be prohibitive in a coupled three-dimensional Earth System Model. In the remainder of this section we summarize our main findings and outline the path forward.

4.1 Principal findings

4.1.1 Validated model components

Each component of the modeling framework has been validated against independent references. The stratospheric transport module reproduces the observed latitudinal structure of Age-of-Air (AoA) inferred from CO_2 and SF_6 measurements, and the tropical AoA vertical profile from previous reanalysis simulations (Chabrillat et al., 2018), with fidelity comparable to three-dimensional Lagranto trajectory calculations. The base-function layer comparison against Lagranto 3-D trajectories (Sun et al., 2024) across 24 single-point injection scenarios (Figs. 4 and 5) shows quantitative agreement (within $\approx 20\%$) for injections at the higher-altitude grid levels (40 and 65 hPa) at all latitudes and for tropical and mid-latitude lower-stratospheric injections, and identifies a genuine limitation of the 2-D framework for lower-stratospheric injections at high latitudes (where the 2-D global burden undershoots Lagranto by up to $\sim 40\%$). This shortfall is attributable to the linearization of eddy perturbations built into the residual-circulation closure (Andrews et al., 1987), which breaks down at the polar vortex edge where the eddy field is non-linear due to Rossby wave breaking. The aerosol microphysics module reproduces the mass-fraction evolution computed by the AER-2D model (Weisenstein et al., 2015) across injection rates spanning 1 to 8 Tg yr^{-1} for a 240 nm monomer radius (Fig. 2), providing confidence in the coagulation and sedimentation scheme. The modified RRTMG radiative transfer scheme agrees with detailed MODTRAN calculations using 64 scattering moments for a representative silica aerosol layer (Fig. 3; Appendix B), validating the treatment of forward/backward scattering asymmetry for highly backscattering aerosols. The Mie/volume-equivalent-sphere treatment of aggregate optical properties is supported by Discrete Dipole Approximation (DDA) simulations on representative aggregate geometries (Appendix B6), which show only a small error in the solar-spectrum-weighted backscattering efficiency and a still smaller error in the longwave absorption, where the longer wavelengths are less sensitive to aggregate geometry.

4.1.2 The residence-time/coagulation trade-off

Tropical injections place particles in the ascending branch of the Brewer–Dobson circulation, which lifts them to higher altitudes and forces them through a long meridional transit before they reach the tropopause sink at higher latitudes; this lengthened circulation path lengthens the aerosol residence time despite the higher sedimentation velocities encountered at the lower air densities aloft (Schoeberl et al., 2025). However, the same tropical confinement that extends residence time also elevates local particle number densities, and therefore amplifies coagulation rates (which scale as the square of particle density). Coagulation produces aggregates with larger effective diameters, which in turn settle faster, partially offsetting the lifetime gain expected from the favorable circulation (Fig. 6, panels b and c). In our calculations this coagulation penalty reduces, but does not eliminate, the residence-time advantage of tropical injection. The net effect is that tropical injections still yield the largest total column burden per unit injection rate for the particle sizes and materials considered in this study.

https://doi.org/10.5194/egusphere-2026-2772
Preprint. Discussion started: 27 May 2026

The fractal morphology of aggregates enters this same residence-time picture almost entirely through the sedimentation velocity. The direct comparison of $D_f = 1.6$ (chain-like aggregates) and $D_f = 3.0$ (compact spheres) at otherwise identical microphysics (Fig. 7) shows a residence-time gain for the loose aggregates of up to $\sim 40\%$ in the tropical pipe, with a $\sim 10\%$ median enhancement, and a comparable amplification of the effective aggregate diameter. This confirms the finding of Weisenstein et al. (2015) that aggregate shape acts on SAI performance primarily through its effect on the sedimentation velocity.

4.1.3 Forcing efficacy, stratospheric heating, and the role of material properties

The radiative forcing efficacy ϵ (Eq. 1; Fig. 11a) is maximized by injection into the tropical pipe, where the longest residence time and the largest insolation overhead combine. The mass-normalized efficiency depends on the effective particle diameter and therefore on the interplay between monomer size and coagulation: under coagulation the $d_0 = 0.3$ μm silica monomer outperforms the $d_0 = 0.5$ μm monomer across most of the tropical lower stratosphere (Fig. 10b), because aggregation grows the 0.3 μm monomers into aggregates of comparable size to those formed by 0.5 μm monomers, placing both at a similar position within the Mie regime, while the 0.3 μm monomers retain a substantial advantage in lifetime. The ϵ map and the lifetime map (Fig. 6) together constitute the principal performance diagnostics that this framework is designed to produce.

The same tropical pipe that maximises ϵ also pays the largest in-layer heating penalty η_{heating} (Eq. 2; Fig. 11c), so cooling efficacy and heating cost trade off spatially across the injection grid (Wells et al., 2024; Bednarz et al., 2023a). The amplitude of this trade-off is set by the choice of injection material through its complex refractive index, which controls both shortwave scattering and longwave absorption. The comparison between silica at $d_0 = 0.5$ μm and calcite at $d_0 = 0.3$ μm, both with coagulation, (Fig. 11, Table 1) shows that calcite's heating cost stays below $0.36\ \mathrm{K\,(W\,m^{-2})^{-1}}$ across the entire grid, reflecting its near-Rayleigh longwave absorption (Keith et al., 2016), while silica pays a substantial heating penalty of up to $2.2\ \mathrm{K\,(W\,m^{-2})^{-1}}$ peaking in the tropical pipe. The magnitude of this inter-material difference is a robust output of the framework, since it does not depend on details of the circulation or microphysics.

The present work reports radiative-forcing efficacy and lower-stratospheric heating directly, with the surface-temperature response estimated only through an assumed climate-sensitivity value (Eq. 3) rather than from a full climate-response calculation; translating the SARF maps into zonal-mean surface-temperature changes via a dedicated 2-D climate-response calculation is planned for future work (Sect. 4.3).

4.1.4 Role of injection schedule

Switching from symmetric (year-round, both hemispheres) to seasonal (alternating-summer-hemisphere) injection at the same total annual rate produces a modest gain in radiative forcing efficacy of ~ 10–20% across the mid-latitude lower stratosphere for both silica and calcite (Fig. 12; Fig. 13). The local-summer pulse builds a higher peak burden than the year-round baseline, because the tropopause is at its highest and the descending branch of the Brewer–Dobson circulation is at its weakest. For silica, this also results in more in-layer warming than additional surface cooling, raising η_{heating} by ~ 0.1–$0.4\ \mathrm{K\,(W\,m^{-2})^{-1}}$ across the mid-latitude band. Beyond the schedule comparison, the meridional shape of the SARF is set primarily by injection

https://doi.org/10.5194/egusphere-2026-2772
Preprint. Discussion started: 27 May 2026

latitude (Fig. 13). This latitudinal degree of freedom appears to provide sufficient flexibility to tailor the meridional RF distribution, including the hemispheric asymmetry that safety- and controllability-driven SAI design demands. The pattern-effect consequences of this RF shape on surface temperature and the hydrological cycle, which determine whether this latitudinal flexibility translates into a comparable degree of freedom in the climate response, will be studied in future work (Sect. 4.3).

4.2 Conclusions and implications

The parameter survey points to a small number of robust design conclusions for solid-particle SAI. Tropical injection maximizes radiative-forcing efficacy by exploiting the long residence times of the tropical pipe, but pays the largest in-layer heating penalty by concentrating the absorbing mass over the same region (Sect. 3.3); coagulation in this confinement amplifies aggregate diameters and partially offsets the mean lifetime advantage (Sect. 3.2.1). Material choice reshapes the trade-off far more than injection geometry: calcite's negligible infrared absorption keeps the in-layer heating penalty an order of magnitude below silica across every injection strategy considered, whereas for an IR-absorbing material such as silica, symmetric mid-latitude injection reduces stratospheric heating with only a limited loss of efficacy.

An alternating-summer-hemisphere seasonal schedule delivers a modest ~ 10–20% mid-latitude gain in radiative-forcing efficacy over symmetric mid-latitude injection, but at a comparable mid-latitude heating-cost penalty (Sect. 3.4). Taken together, the results imply that solid-particle SAI evaluations should not be reduced to a single figure of merit: the efficacy-versus-heating trade-off is governed by an interplay between particle microphysics, transport, and injection geometry whose qualitative balance depends on the material's infrared absorption profile.

4.3 Future work

Several extensions are planned. First, a stratospheric ozone-chemistry module will be added, including the heterogeneous reactions currently considered most relevant for silica and coated calcite surfaces, based on ongoing laboratory measurements (Lostier et al, 2026). This will enable a direct ozone-impact comparison with sulfate-based SAI. Second, the idealized lower-boundary treatment of aerosol loss will be replaced by a realistic, wet-deposition-based tropospheric sink that represents in-cloud and below-cloud scavenging once the aerosol is transported into the upper troposphere, eliminating an important systematic uncertainty in the aerosol residence time and enabling the calculation of surface-deposition patterns. Third, an aerosol–radiation–transport feedback loop will be implemented, using the aerosol radiative heating computed by the RRTMG module to update the TEM residual circulation and the diffusion tensor within the 2-D framework. As part of the same coupling effort, a stratospheric water-vapor feedback will be added to capture the influence of tropopause warming on stratospheric water vapor through the Brewer–Dobson cold-trap (Schoeberl et al., 2019). Fourth, the framework will be coupled to a 2-D climate-response model so that the SARF maps produced here can be translated into zonal-mean surface-temperature, hydrological-cycle, and circulation responses at comparable computational cost as the present sweeps. The latitudinal degree of freedom evident in the meridional RF distribution (Fig. 13) already addresses the safety- and controllability-driven hemispheric-asymmetry requirements at the RF level (Waxman et al., 2026); the climate-response coupling will determine whether this flexibility carries through to surface-temperature and hydrological-cycle patterns, providing an intermediate-fidelity step between the radiative-

https://doi.org/10.5194/egusphere-2026-2772
Preprint. Discussion started: 27 May 2026

forcing maps and full 3-D climate response. Fifth, the most favorable efficacy/heating trade-off regions identified in the 2-D sweeps will be explored with coupled three-dimensional Community Earth System Model (CESM - Danabasoglu et al. (2020)) for validation of the transport–microphysics–radiation coupling and for the assessment of regional climate response.

Code and data availability. A public repository hosting the code and data required to reproduce the results of this study is under preparation at [https://github.com/stardust-initiative/solid-sai-2d-paper]. This repository will serve as the entry point and link to a set of component repositories containing the simulation codes, configuration files, post-processing scripts, and the numerical data underlying all figures in this paper. All materials will be deposited in a citable archive (Zenodo) and assigned persistent DOIs prior to final publication. During peer review, the authors will provide reviewers with access to current versions of these materials upon request through the editorial office.

Appendix A: Eddy diffusion tensor and residual circulation from ERA5

The advection–diffusion form of the zonally averaged tracer transport equation, with mean advection by the residual circulation $(v_{\mathrm{res}}, \omega_{\mathrm{res}})$ and effective diffusivity (Haynes and Shuckburgh, 2000) modeled via a symmetric diffusion tensor $\mathbf{D}$, follows the standard Transformed Eulerian Mean (TEM) derivation (Andrews and McIntyre, 1976; Dunkerton, 1978; Holton, 1981) and is reproduced unmodified in our model. The substantive task is to determine $\mathbf{D}$, v_{res}, and ω_{res} from ERA5 data; we do so via the displacement parametrization of Holton (1981), which represents the eddy contribution to the tracer flux through an eddy-displacement vector (η^*, ξ^*) that obeys

$$\frac{D}{Dt}\begin{pmatrix}\eta^* \\ \xi^*\end{pmatrix} = \begin{pmatrix}v' \\ \omega'\end{pmatrix}, \tag{A1}$$

where D/Dt is the material derivative and v', ω' are the deviations from the zonal-mean velocity. Equation (A1) is solved numerically by semi-Lagrangian backward tracing through the full three-dimensional ERA5 wind field (u, v, ω), using the native 137 model-level data subsampled to 3-hourly output on a $1^\circ \times 1^\circ$ horizontal grid. Only levels in the 1–500 hPa range are retained (~ 81 levels). At each time step the displacement fields are interpolated to the departure points (trilinear in (λ, φ, p)) and incremented by $v'\,\Delta t$ and $\omega'\,\Delta t$.

The diffusion-tensor components are then computed as zonal-mean correlations between the eddy velocities and the displacement fields, yielding the symmetric diffusion tensor

$$\mathbf{D} = \begin{pmatrix} \overline{v'\eta^*} & \frac{1}{2}\left(\overline{v'\xi^*} + \overline{\omega'\eta^*}\right) \\ \frac{1}{2}\left(\overline{v'\xi^*} + \overline{\omega'\eta^*}\right) & \overline{\omega'\xi^*} \end{pmatrix}, \tag{A2}$$

together with an antisymmetric part that recovers the eddy-induced residual advection consistent with the TEM closure. The tensor components are time-averaged over each calendar month and then over the ten-year period 2008–2017 to give the monthly mean climatology used in the model.

https://doi.org/10.5194/egusphere-2026-2772
Preprint. Discussion started: 27 May 2026

For numerical robustness in the stratosphere, four post-processing steps are applied to the raw $(\Psi, \mathbf{D})$ fields. (i) For advection we use the TEM residual stream function $\Psi_{\mathrm{res,TEM}} = -\int v_{\mathrm{res}}\, dp$ rather than the displacement-based $\Psi_{\mathrm{displ}} = -\frac{1}{2}(K_{\varphi p} - K_{p\varphi})$: a per-timestep signal-to-noise analysis (ratio of temporal standard deviation to absolute mean) shows that the difference between the two, $\Psi_{\mathrm{corr}} = \Psi_{\mathrm{displ}} - \Psi_{\mathrm{TEM}}$, exceeds noise ratio unity in more than 95% of the stratospheric domain above 100 hPa, while $\Psi_{\mathrm{res,TEM}}$ remains robust throughout. (ii) For the same reason the symmetric off-diagonal element $D_{\varphi p} = \frac{1}{2}(K_{\varphi p} + K_{p\varphi})$, whose noise ratio exceeds unity in over 90% of the stratospheric domain, is set to zero, leaving a purely diagonal symmetric diffusion tensor $\mathbf{D} = \mathrm{diag}(D_{\varphi\varphi}, D_{pp})$. The physical effect of the off-diagonal coupling, tilted mixing along isentropic surfaces, is partially captured by the TEM residual advection. (iii) Sub-grid-scale mixing floors are imposed: $D_{\varphi\varphi}^{\mathrm{floor}} = 10^4\ \mathrm{m^2\,s^{-1}}$ for the meridional diffusivity, and a height-dependent vertical floor $D_{pp}^{\mathrm{floor}}(p) = K_{zz}^{\mathrm{floor}}\, p^2/H^2$ derived from $K_{zz}^{\mathrm{floor}} = 10^{-2}\ \mathrm{m^2\,s^{-1}}$ with scale height $H \approx 7000$ m. (iv) Poleward of $85°$, the eddy-induced velocities (which involve $1/\cos\varphi$ factors) are masked and filled by linear interpolation along latitude from the nearest valid mid-latitude values; the physical boundary conditions $v = 0$, $\omega = 0$, $\Psi = 0$ are then enforced at $\pm 90°$.

A1 Numerical solver for the tracer transport equation

The advection–diffusion form of the tracer transport equation, recast in $(y = a\sin\phi, p)$ coordinates, is integrated by directional splitting of the advective and diffusive operators. Advection uses the flux-form, mass-conserving NIRVANA scheme (Leonard et al., 1995) with quadratic interpolation of the cell-edge tracer integral and monotonicity limiters following Gregory and West (2002); this places it in the same family of non-diffusive, mass-conserving flux-form semi-Lagrangian schemes as Lin and Rood (1996). The cross-derivative diffusion terms are handled by effective advective velocities following Western et al. (2024). Time stepping uses a Courant-limited adaptive step (advective $C_A = 0.25$, diffusive $C_K = 0.5$); zero-flux boundary conditions are applied at all domain boundaries.

A2 Seasonal climatology of transport coefficients

Figure A1 compares two independent estimates of the seasonal mean meridional diffusion coefficient $D_{\varphi\varphi}$. The top row is our derivation from ERA5 reanalysis (10-year climatology, 2008–2017) following the procedure described above; the bottom row is the GSFC 2-D model field (Fleming et al., 1999) for the year 2000.

$D_{\varphi\varphi}$ exhibits the familiar two-regime structure of the stratospheric meridional eddy diffusivity: low values throughout the tropical pipe (Plumb, 1996), surrounded by a winter-hemisphere mid-latitude "surf zone" (McIntyre and Palmer, 1983) where breaking planetary waves produce the dominant maxima. The seasonal cycle is the expected one, with the NH winter maximum strongest in DJF and the SH winter–spring maximum strongest in SON. Our derivation and the GSFC 2-D model agree closely in the location, seasonal cycle, and amplitude of the surf-zone maxima and of the tropical-pipe minima. The main qualitative difference is that our reanalysis-based derivation shows somewhat sharper gradients at the edges of the winter polar vortex, consistent with its higher horizontal resolution compared with the smoothing inherent to a tuned 2-D fit.

The TEM residual stream function $\Psi_{\mathrm{res,TEM}}$ (Fig. A2) represents the Brewer–Dobson circulation, with the NH cell strongest in DJF and the SH cell strongest in JJA.

https://doi.org/10.5194/egusphere-2026-2772
Preprint. Discussion started: 27 May 2026

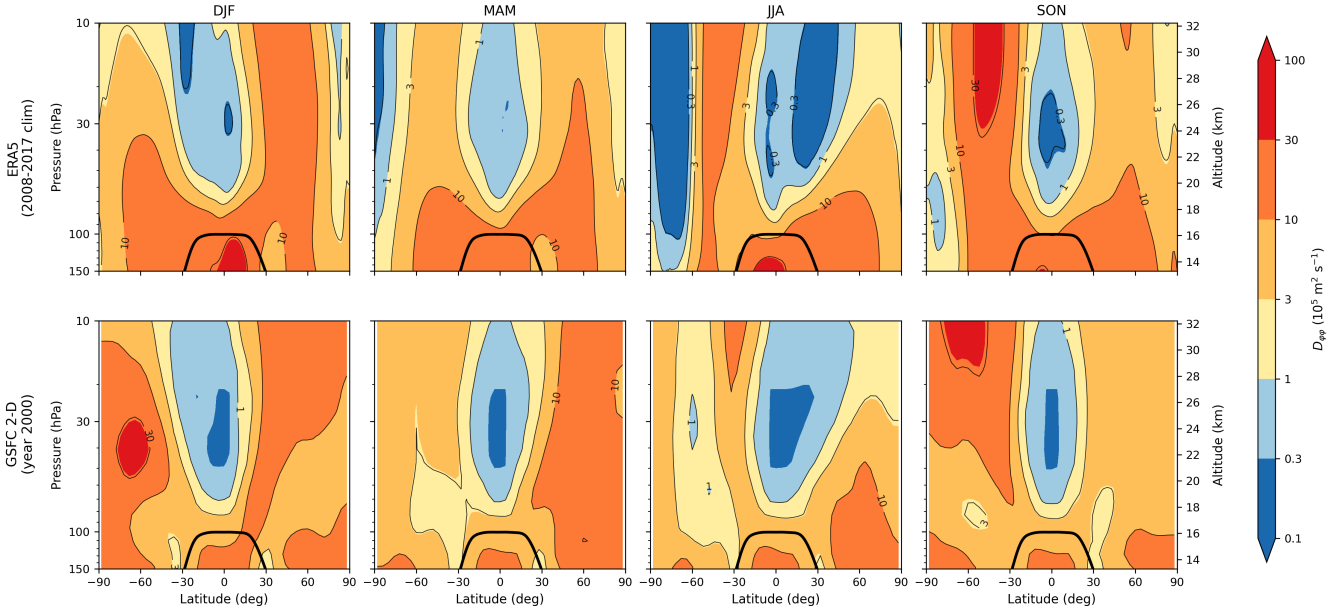

Figure A1. Seasonal mean meridional diffusion coefficient $D_{\varphi\varphi}$ for DJF, MAM, JJA, and SON (columns left to right), shown on a log scale in units of $10^5\ \mathrm{m^2\,s^{-1}}$. Top row: this work, derived from ERA5 reanalysis (10-year climatology, 2008–2017). Bottom row: GSFC 2-D model (Fleming et al., 1999), courtesy of E. L. Fleming (private communication). The black line in each panel marks the ERA5 climatological tropopause; the right-hand axis on the rightmost column gives the approximate altitude in km. Pressure range: 10–150 hPa.

Appendix B: Modeling the radiative response of an aerosol layer

B1 Radiative forcing of a stratospheric aerosol layer

The longitudinally integrated planar radiative transfer equation has the form

$$\mu\frac{dI^+(\tau,\mu)}{d\tau} = I^+(\tau,\mu) - \frac{1}{2}\omega\int_0^1 d\mu'\left(P(\mu,\mu')I^+(\tau,\mu') + P(\mu,-\mu')I^-(\tau,\mu')\right),$$

$$-\mu\frac{dI^-(\tau,\mu)}{d\tau} = I^-(\tau,\mu) - \frac{1}{2}\omega\int_0^1 d\mu'\left(P(\mu,-\mu')I^-(\tau,\mu') + P(\mu,-\mu')I^+(\tau,\mu')\right). \quad \text{(B1)}$$

https://doi.org/10.5194/egusphere-2026-2772
Preprint. Discussion started: 27 May 2026

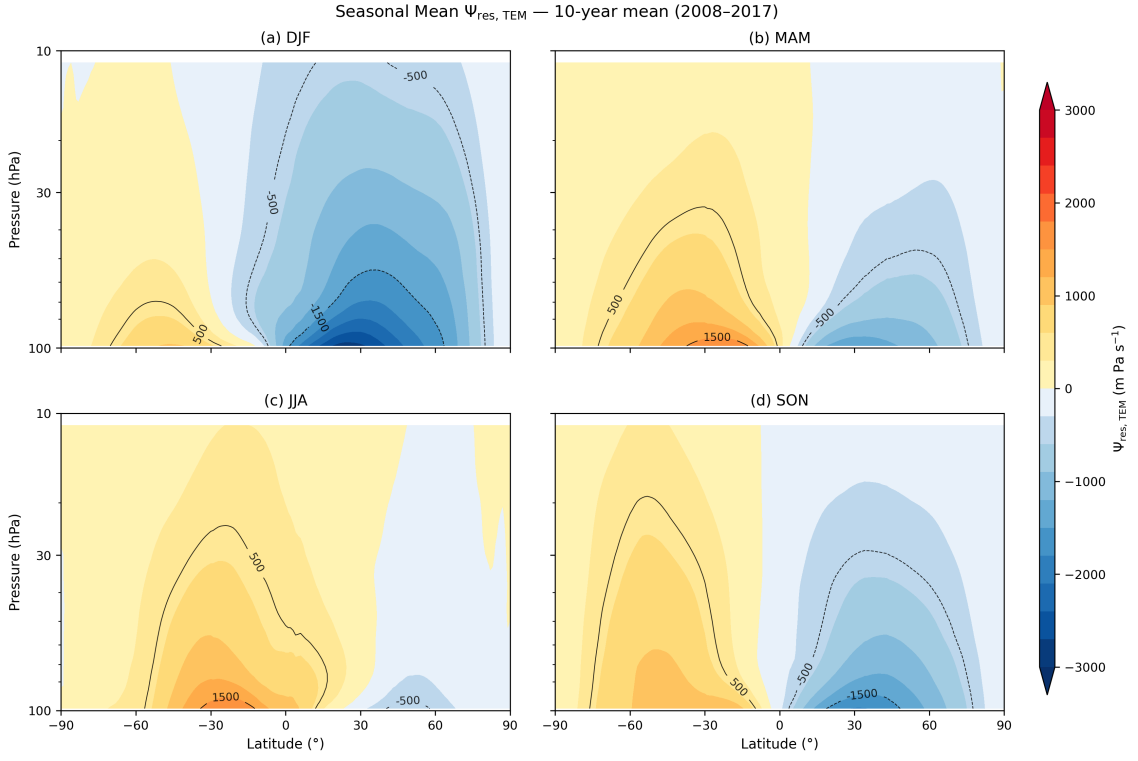

Figure A2. Seasonal mean TEM residual stream function $\Psi_{\mathrm{res,TEM}} = -\int v_{\mathrm{res}}\, dp$ (m Pa s^{-1}) for (a) DJF, (b) MAM, (c) JJA, and (d) SON, derived from ERA5 reanalysis (10-year climatology, 2008–2017) and representing the Brewer–Dobson circulation. Black contours mark the ± 500 and ± 1500 m Pa s^{-1} isolines. Pressure range: 10–100 hPa (log scale).

Here $I^{\pm}(\tau,\mu)$ denote the up-going/down-going intensities $I(\tau,\pm\mu)$ with $0 \le \mu \le 1$, and $\overline{P}(\mu,\mu')$ is the azimuthally integrated phase function

$$\overline{P}(\mu,\mu') \equiv \frac{1}{\pi}\int_0^{\pi} P\big(\mu\mu' + (1-\mu^2)^{1/2}(1-\mu'^2)^{1/2}\cos\phi\big)\, d\phi, \tag{B2}$$

which satisfies the normalizations $\frac{1}{2}\int_{-1}^{1}\overline{P}(\mu,\mu')\,d\mu' = 1$ and $\frac{1}{2}\int_0^{\pi} P(\cos\Theta)\sin\Theta\, d\Theta = 1$, with the scattering angle Θ given by $\cos\Theta = \mu\mu' + (1-\mu^2)^{1/2}(1-\mu'^2)^{1/2}\cos\phi$.

The case of a mono-directed down-coming beam heating a layer of optical depth τ is characterized by a zenith angle $\mu_0 = \cos\theta_0$ and boundary conditions $I^-(0,\mu') = F\delta(\mu'-\mu_0)$, $I^+(\tau,\mu') = 0$. Solving for the up-scattered $I^+(0,\mu)$ from the top of the layer in the thin limit gives $I^+(0,\mu) = F\tau\omega/(2\mu)\, P(\mu,-\mu_0)$.

Denoting $\beta(\mu_0) \equiv \frac{1}{2}\int_0^1 d\mu\, P(\mu,-\mu_0)$ as the back-scattering fraction of the mono-directional radiation and ω as the single scattering albedo, and adding a wavelength subscript λ where it had been suppressed for clarity, the fraction of mono-directional

https://doi.org/10.5194/egusphere-2026-2772
Preprint. Discussion started: 27 May 2026

flux reflected in the vertical direction is

$$r_\lambda(\mu_0) = \frac{\tau_\lambda\,\omega_\lambda\,\beta_\lambda(\mu_0)}{\mu_0}, \tag{B3}$$

and the fraction of mono-directional radiation absorbed in the layer is

$$a_\lambda(\mu_0) = \frac{1-\omega_\lambda}{\mu_0}\,\tau_\lambda. \tag{B4}$$

The corresponding diffuse-isotropic coefficients, obtained from the solar-flux-weighted integration of $r_\lambda(\mu_0)$ and $a_\lambda(\mu_0)$ over the full hemisphere, are

$$\overline{r_\lambda} = 2\,\overline{\beta_\lambda}\,\omega_\lambda\,\tau_\lambda, \quad \overline{a_\lambda} = 2(1-\omega_\lambda)\,\tau_\lambda, \tag{B5}$$

with $\overline{\beta_\lambda} = \int_0^1 \beta_\lambda(\mu)\,d\mu$, which can be evaluated as a single integral over the scattering angle (Wiscombe and Grams, 1976). We similarly define the mono-directional and diffuse transmission coefficients $t_\lambda(\mu_0) = 1 - r_\lambda(\mu_0) - a_\lambda(\mu_0)$ and $\overline{t_\lambda} = 1 - \overline{r_\lambda} - \overline{a_\lambda}$. Up to this point the derivation follows Coakley and Chylek (1975) and Wiscombe and Grams (1976).

Accounting for multiple reflections from a surface of effective albedo α_λ (combining the surface and the atmosphere below the layer), the total reflection of the layer + surface system is

$$R_\lambda = r_\lambda(\mu_0) + \frac{\alpha_\lambda\,\overline{t_\lambda}\,t_\lambda(\mu_0)}{1-\alpha_\lambda\,\overline{r_\lambda}}, \tag{B6}$$

and the resulting instantaneous radiative forcing of the layer (referred to here as the layer-model RF) is

$$\mathrm{RF}(\lambda) = \Big(R_\lambda - \alpha_\lambda\Big)\,S_\lambda. \tag{B7}$$

B2 Consistent choice of zenith angle and scattering efficiency

The cosine of the solar zenith angle μ_0 in Eq. B6 is instantaneous; in our model we average over the diurnal cycle and reduce the problem to the two-stream formalism solved within RRTMG. The instantaneous cosine of the zenith angle at latitude φ and angular hour h (both in radians) is $\mu_{\delta,\varphi}(h) = \max\{\sin\varphi\sin\delta + \cos\varphi\cos\delta\cos h, 0\}$, where δ is the Earth's inclination angle, and the daylight hour-angle is set by $\cos h_0(\varphi,\delta) = -\tan\varphi\tan\delta$. We choose an effective $\mu_{\delta,\varphi} = \overline{\mu_{\delta,\varphi}(h)}^{\,\eta}$ via some averaging method η. Examples are the daily and insolation-weighted means

$$\begin{aligned}
\overline{\mu_{\delta,\varphi}(h)}^{\,\mathrm{daily}} &= \frac{1}{2\pi}\int_{-h_0}^{h_0} dh\,\mu_{\delta,\varphi}(h), \\
\overline{\mu_{\delta,\varphi}(h)}^{\,Q} &= \frac{\int_{-h_0}^{h_0} dh\,\mu^2_{\delta,\varphi}(h)}{\int_{-h_0}^{h_0} dh\,\mu_{\delta,\varphi}(h)}.
\end{aligned} \tag{B8}$$

Once an averaging method η is chosen, the consistent formulation of the rest of the radiative response of the aerosol layer follows from the requirement that the directional and isotropic reflected/absorbed powers are correctly described over a full 24-hour period. The mono-directional reflected and absorbed fluxes, $F_{\lambda,\mathrm{scat,dir}}(h,\delta,\varphi) = \beta_\lambda(\mu_{\delta,\varphi}(h))\,\omega_\lambda\,\tau_\lambda\,S_{\lambda,0}$ and

https://doi.org/10.5194/egusphere-2026-2772
Preprint. Discussion started: 27 May 2026

$F_{\lambda,\mathrm{abs,dir}}(h,\delta,\varphi) = (1-\omega_\lambda)\,\tau_\lambda\,S_{\lambda,0}$, dictate that $\beta_\lambda(\mu)$ be averaged over the full daylight period, while the constant absorbed-flux right-hand side carries an overall h_0/π factor (the ratio of daylight to the 24-hour cycle). The diffuse-flux variants follow from the small-τ expansion of Eq. B5 and of the corresponding absorption. The combined averaging-consistent layer-model coefficients are

$$
\begin{aligned}
r_\lambda(\delta,\varphi) &= \frac{\overline{\beta_\lambda(\mu_{\delta,\varphi})}^{\mathrm{daily}}}{\overline{\mu_{\delta,\varphi}}^{\eta}}\,\omega_\lambda\,\tau_\lambda,\\
a_\lambda(\delta,\varphi) &= \frac{1}{\overline{\mu_{\delta,\varphi}}^{\eta}}\,\frac{h_0(\delta,\varphi)}{\pi}\,(1-\omega_\lambda)\,\tau_\lambda,\\
\overline{r}_\lambda(\delta,\varphi) &= f_{\delta,\varphi}\cdot 2\,\overline{\beta_\lambda}\,\omega_\lambda\,\tau_\lambda,\\
\overline{a}_\lambda(\delta,\varphi) &= f_{\delta,\varphi}\cdot 2(1-\omega_\lambda)\,\tau_\lambda,
\end{aligned}
\tag{B9}
$$

where $f_{\delta,\varphi} \equiv \overline{\mu_{\delta,\varphi}}^{\mathrm{daily}}/\overline{\mu_{\delta,\varphi}}^{\eta}$ is a correction factor.

B3 Modification of RRTMG for a Mie-scattering aerosol layer

RRTMG (Mlawer et al., 1997; Clough et al., 2005; Oreopoulos et al., 2012) is an open-source two-stream radiation scheme widely used in GCMs, including CESM. Spectrally it employs 16 long-wave (LW) and 14 short-wave (SW) bands with several g-points per band in a correlated-k framework, and solves for the upward and downward fluxes column by column. LW is treated in the absorption-only limit; in SW, each cell is described by its optical depth τ, single-scattering albedo ω, and asymmetry factor g. RRTMG was validated against line-by-line calculations by Oreopoulos et al. (2012) and performs well for the GCM use cases of clouds and broad-band gaseous scattering. In this work we access RRTMG through the `climlab-rrtmg` wrapper (Rose and climlab contributors, 2024), a Python package that exposes the Fortran RRTMG driver as part of the climlab modeling framework (Rose, 2018).

The SW two-stream core of RRTMG follows Welch et al. (1980) and uses a closed form of the back-scattering fraction $\beta(\mu)$ that is linear in μ, with g as the sole tuning parameter. This parametrization is adequate for its intended use but cannot capture the Mie-regime back-scattering of sub-micron particles, in a zonally averaged framework. A direct attempt to represent the aerosol layer by its Mie-derived (τ,ω,g) and letting RRTMG compute its own two-stream coefficients is therefore inadequate, and the resulting bias is visible in Fig. 3.

To reconcile the layer-model description of Sect. B2 with the RRTMG two-stream solver, we modified the `reftra_sw` subroutine of the RRTMG-SW code, which, within each (sub-)column of the McICA decomposition, computes the per-layer reflection and transmission coefficients that are subsequently combined by the adding-doubling procedure. For any layer that overlaps the aerosol burden and that does *not* itself contain a cloud in the current sub-column, the baseline RRTMG direct-beam coefficients $(r^{(\mathrm{dir})},t^{(\mathrm{dir})})$ and diffuse coefficients $(r^{(\mathrm{diff})},t^{(\mathrm{diff})})$ are each augmented by the matching layer-model coefficients

https://doi.org/10.5194/egusphere-2026-2772
Preprint. Discussion started: 27 May 2026

in the two channels:

$$
\begin{aligned}
r^{(\mathrm{dir})} &\to 1 - \big(1 - r^{(\mathrm{dir})}\big)\,\big(1 - r_\lambda(\mu_0)\big),\\
t^{(\mathrm{dir})} &\to t_\lambda(\mu_0)\, t^{(\mathrm{dir})},\\
r^{(\mathrm{diff})} &\to 1 - \big(1 - r^{(\mathrm{diff})}\big)\,\big(1 - \overline{r}_\lambda\big),\\
t^{(\mathrm{diff})} &\to \overline{t}_\lambda\, t^{(\mathrm{diff})}.
\end{aligned}
\tag{B10}
$$

Here $(r_\lambda(\mu_0), t_\lambda(\mu_0))$ and $(\overline{r}_\lambda, \overline{t}_\lambda)$ are, respectively, the directional and diffuse layer-model coefficients defined in Sect. B2, evaluated consistently with the chosen diurnal averaging convention η. The four layer-model coefficients are spectrally averaged onto the 14 RRTMG SW bands using a solar-irradiance weighting, and the Mie calculation itself uses the relevant aerosol material's complex refractive index. Layers in which the aerosol burden co-exists with a cloud in the current sub-column retain the nominal RRTMG treatment; this avoids imposing an untested cloud–aerosol coupling at the radiative-transfer level. The remainder of the RRTMG SW calculation (the adding-doubling across layers, gaseous absorption, and the δ-scaling of g) is unchanged (code is available through the `climlab-rrtmg_stardust` repository).

The modified RRTMG thus feeds the two-stream solver with per-layer reflection/transmission coefficients that already encode the layer-model physics, while inheriting the spectral bands, gaseous absorption, and surface treatment of the original RRTMG verbatim. In retrospect, the resulting scheme can be read as a hybrid of the thick- and thin-atmosphere two-stream formulations reviewed in Ho and Pincus (2024): the RRTMG part supplies the standard Zdunkowski-type adding-doubling treatment of the thick atmosphere, while the injected layer-model coefficients correspond to the Coakley–Chylék thin-layer limit in which the aerosol optical depth is small and the non-linear $\beta(\mu)$ behavior is treated analytically.

B4 Longwave treatment

The longwave channel of RRTMG is used without any `reftra`-style modification. For dielectric aerosols in the size range relevant to solid-aerosol stratospheric injection (radii from $\sim$ 200 nm up to $\sim$ 2–3 μm, with the upper end set by the competition between coagulation growth and gravitational settling that removes larger particles from the stratosphere; see Sect. 2.2), the size parameter $x = 2\pi r/\lambda$ across the thermally relevant RRTMG LW bands is well below unity. In this small-particle limit, scattering is negligible compared to absorption, and RRTMG's native pure-absorption LW treatment is therefore the correct leading-order description. Because the LW response of a thin layer is also linear to leading order in both the Planck function and the layer optical depth, and the Planck function is smooth over the modest longitudinal temperature variations at a given stratospheric altitude, the zonal-mean temperature field of the 2-D transport model carries over to the LW calculation without a non-linearity correction analogous to the SW averaging of Sect. B2. A formal LW-side comparison of the modified RRTMG against MODTRAN, covering both fluxes and heating rate profiles, is nevertheless left for future work.

https://doi.org/10.5194/egusphere-2026-2772
Preprint. Discussion started: 27 May 2026

B5 Optical properties of explored materials

To compare the SAI-relevant optical performance of the two discussed aerosol materials - silica and calcite - we compute the Mie scattering and absorption efficiencies of a single homogeneous spherical particle using `miepython` (Prahl). For each material and effective particle diameter we evaluate the unpolarized scattering phase function $P_\lambda(\mu)$ and integrate to obtain the backscattered fraction for isotropically incident radiation

$$\bar{\beta}(d_{\rm eff},\lambda) \;=\; \frac{1}{2\pi}\int_{-1}^{+1} P_\lambda(\mu)\arccos(\mu)\,d\mu, \tag{B11}$$

where $P_\lambda(\mu)$ is the unpolarized Mie phase function at wavelength λ normalized so that $\int P_\lambda\,\mathrm{d}\Omega = 4\pi$. Throughout this appendix $\bar{\beta}(d_{\rm eff},\lambda)$ denotes the phase-function-derived backscatter factor of Eq. (B11) – it is *not* a spectral average; spectrum-weighted averages are written as $\langle\cdot\rangle_{\rm SW}$ or $\langle\cdot\rangle_{\rm LW}$ throughout. The Mie scattering and absorption efficiencies follow the Bohren & Huffman convention $Q_{\rm sca}(d_{\rm eff},\lambda) \equiv 4\sigma_{\rm sca}/(\pi d_{\rm eff}^2)$ and $Q_{\rm abs}(d_{\rm eff},\lambda) \equiv 4\sigma_{\rm abs}/(\pi d_{\rm eff}^2)$.

The two figure panels in Fig. B1 report spectrum-integrated efficiencies on two different spectral weights:

- Panel (a): *shortwave* backscatter efficiency $\langle\bar{\beta}\,Q_{\rm sca}\rangle_{\rm SW}$, integrated against a solar Planck spectrum at $T_{\rm sw} = 6000\,\mathrm{K}$ on $\lambda \in [0.25, 4]\,\mu\mathrm{m}$ (UV cutoff at $0.25\,\mu\mathrm{m}$ representing the atmospheric ozone absorption).
- Panel (b): *longwave* absorption efficiency $\langle Q_{\rm abs}\rangle_{\rm LW}$, integrated against a piecewise-Planck spectrum split at the wavenumber edges $\{600, 800, 1250\}\,\mathrm{cm}^{-1}$ with brightness temperatures $\{255, 220, 290, 255\}\,\mathrm{K}$ on each window, to represent the far-IR / CO_2-15 μm / atmospheric-window / near-IR portions of the terrestrial outgoing longwave spectrum.

For a Mie sphere of effective diameter $d_{\rm eff}$, the backscatter cross-section per unit material volume is

$$\frac{\sigma_b}{V} \;=\; \frac{3}{2}\,\frac{\bar{\beta}\,Q_{\rm sca}}{d_{\rm eff}}\;\;[\mu\mathrm{m}^{-1}], \tag{B12}$$

and the same factor $3/(2d_{\rm eff})$ is applied to $Q_{\rm abs}$ for panel (b). Reporting σ/V instead of the bare dimensionless efficiency directly expresses the per-volume optical activity of the aerosol material. For Fig. B1 we set $d_{\rm eff} = d_0 = 500\,\mathrm{nm}$ so both materials are compared at the same monomer size.

Material-specific complex refractive indices $n(\lambda) + i\,k(\lambda)$ are used over the full computation range:

- **Amorphous silica (SiO_2, $\rho = 2200\,\mathrm{kg\,m^{-3}}$)**: Kitamura et al. (2007) optical constants, spanning extreme UV to far-IR at near-room temperature.
- **Calcite ($CaCO_3$, $\rho = 2710\,\mathrm{kg\,m^{-3}}$)**: Long et al. (1993) Lorentz oscillator fit to crystalline reflectance measurements (separate ordinary-ray and extraordinary-ray fits) for the IR phonon resonances; principal-axis averaging convention discussed below.

Calcite principal-axis averaging: Calcite is a uniaxial birefringent crystal, with distinct ordinary and extraordinary refractive indices ($n_o = 1.658$, $n_e = 1.486$ at the sodium line $\lambda = 589.3\,\mathrm{nm}$). Stratospheric calcite particles in an SAI deployment

https://doi.org/10.5194/egusphere-2026-2772
Preprint. Discussion started: 27 May 2026

are expected to be either randomly oriented small crystals or partly amorphous; in either case the optical response is dominated by the volume-averaged dielectric tensor. For the Mie calculation we employ the *ray-arithmetic-mean* convention, $m_{\mathrm{RayAvg}}(\lambda) = [m_o(\lambda) + m_e(\lambda)]/2$, applied to the complex refractive index on each axis. This convention matches the simplified principal-axis averaging used in prior SAI work by Dykema et al. (2016); a more rigorous alternative is the Voigt random-orientation effective dielectric $\varepsilon_{\mathrm{eff}} = (2\varepsilon_o + \varepsilon_e)/3$, which shifts the SW backscatter by a few percent . We choose the ray-arithmetic-mean for direct comparability with published solid-aerosol SAI studies.

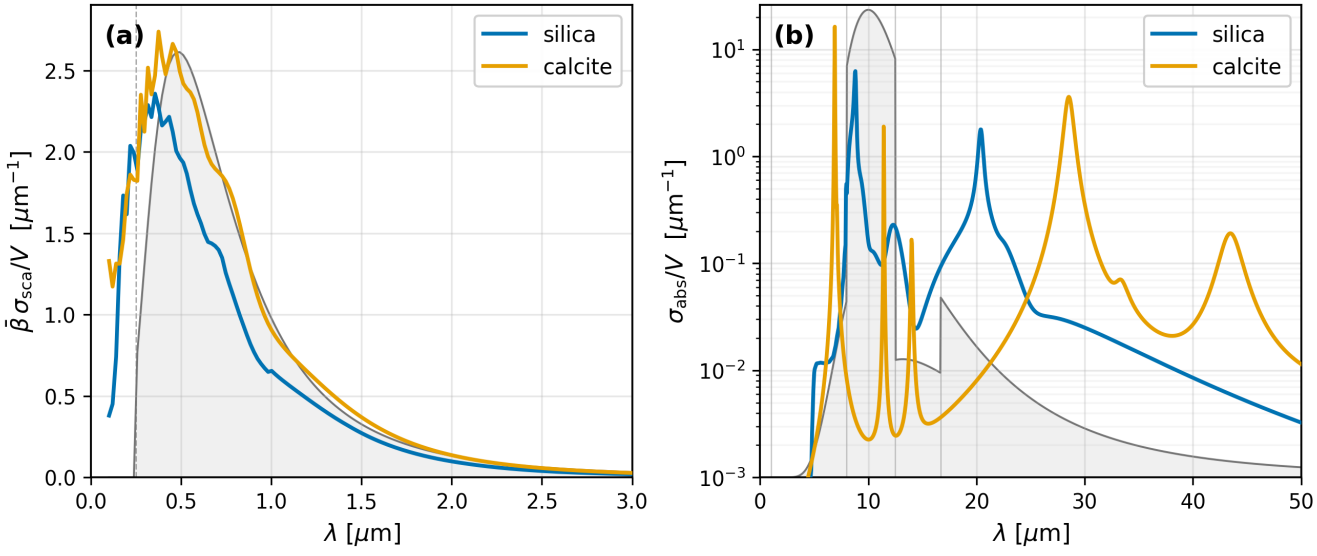

Figure B1. Volume-normalized Mie efficiencies for amorphous silica (blue) and calcite (orange) spheres of monomer diameter $d_0 = 500\,\mathrm{nm}$. (a) Shortwave backscatter $\bar{\beta}\,\sigma_{\mathrm{sca}}/V$ (with $\bar{\beta}$ from Eq. (B11)), solar-Planck-weighted at $T_{\mathrm{sw}} = 6000\,\mathrm{K}$ on $\lambda \in [0.25, 4]\,\mu\mathrm{m}$. (b) Longwave absorption σ_{abs}/V (log-scale), piecewise-Planck weighted across the four thermal-IR bands defined in the text. Notably, silica peak absorption lies within the atmospheric window, while calcite peak absorption lies outside it. Grey shaded curves mark the spectral weighting in each panel.

B6 Optical properties of agglomerates

Particle coagulation in the stratosphere produces aggregate structures whose optical properties may differ from those of equivalent-volume spheres. To quantify this effect, we performed Discrete Dipole Approximation (DDA) simulations (Yurkin and Hoekstra, 2007) comparing the scattering properties of fractal aggregates to those computed using Mie theory for effective spheres.

The DDA simulations were carried out for SiO_2 particles using the complex refractive index of Kitamura et al. (2007), with a monomer radius of $R = 250$ nm and a dipole spacing of $\Delta = 30$ nm. Multiple aggregate morphologies were considered, spanning monomers ($N = 1$), dimers ($N = 2$), trimers ($N = 3$; compact and linear), tetramers ($N = 4$; compact, square,

https://doi.org/10.5194/egusphere-2026-2772
Preprint. Discussion started: 27 May 2026

and linear), and pentamers ($N = 5$; compact, planar, cross, and square pyramid configurations). For each morphology, the orientation-averaged backscattering cross section was computed over 20 orientations.

The key radiative quantity for SAI efficacy is the solar spectrum-weighted backscattering efficiency $\langle \bar{\beta} Q_{\mathrm{sca}} \rangle_{\mathrm{SW}}$, which determines the fraction of incident solar radiation scattered back to space. For each aggregate, the wavelength-dependent product $\bar{\beta}(\lambda) Q_{\mathrm{sca}}(\lambda)$ was computed over the range 300–3000 nm and weighted by the solar irradiance spectrum. The resulting spectrum-weighted values were compared to Mie calculations for an effective sphere of diameter $d_{\mathrm{eff}} = d_0 N^{1/3}$ (i.e., a sphere of equal total volume), normalized per monomer geometric cross section.

Figure B2(a) presents the solar-spectrum-weighted volume-normalized backscatter $\bar{\beta} \sigma_{\mathrm{sca}} / V$ as a function of effective diameter for all morphologies considered, with the corresponding cluster geometries shown in panel (b). The DDA results for all aggregate configurations fall close to the Mie effective-sphere curve (dashed red), with deviations that are small compared to uncertainties in aerosol optical properties and size distributions in the stratosphere.

B7 Stratosphere-Adjusted Radiative Forcing Calculations

We compute the stratosphere-adjusted radiative forcing (SARF) of each prescribed aerosol injection scenario in two steps: (i) a season-specific reference model is integrated to a fixed point under ERA5-pinned tropospheric conditions, and (ii) a perturbed model identical to the reference except for the addition of the prescribed aerosol mass-mixing-ratio profile is integrated with the same pinning until its stratosphere has relaxed radiatively, yielding SARF as the top-of-atmosphere (TOA) net-flux anomaly between, $\mathrm{ASR}_{\mathrm{anom}} - \mathrm{OLR}_{\mathrm{anom}}$, between the perturbed and reference simulations, integrated against per-season radiation backgrounds and averaged over the four calendar seasons. Both steps are initialized with the ERA5 seasonal-mean state (DJF, MAM, JJA, SON; built from the ERA5 monthly climatology of years 2008–2018). The atmospheric temperatures above $p_{\mathrm{trop}} = 175\ hPa$ are allowed to evolve freely under the radiative tendency, with a stratospheric floor of $T_{\mathrm{min}} = 180\,\mathrm{K}$ to suppress polar-night runaway. Similarly, both are integrated until the stratospheric profile has relaxed to its radiative fixed point under the season-specific insolation. Because tropospheric T_{atm}, q, T_s and surface albedo are identical between reference and perturbed runs, SARF isolates the direct radiative effect of the aerosol *plus* the stratosphere-only adjustment that radiative equilibrium requires under the modified absorption profile, while excluding tropospheric feedbacks.

The *tropical lower-stratospheric heating peak*, $\Delta T_{\mathrm{peak,trop}}$, is calculated as the maximum over $|\varphi| \leq 30^\circ$ and over the stratospheric column of the spatially smoothed steady-state temperature anomaly $T_{\mathrm{pert.}} - T_{\mathrm{ref.}}$, where the smoothing is a Gaussian kernel with $\sigma_\varphi = 5^\circ$ and $\sigma_{\ln p} = 0.05$.

Author contributions. YL led the project, wrote the manuscript, and contributed to the computations underlying Appendices A and B. NW developed the transport and coagulation components, implemented them within CLIMLAB, produced the transport results, and contributed to the writing. DH developed the radiative-transfer components, implemented them within CLIMLAB, produced the radiation results, and contributed to the writing. BEJR supervised the CLIMLAB modifications, co-led the scientific direction, and reviewed and edited the manuscript.

https://doi.org/10.5194/egusphere-2026-2772
Preprint. Discussion started: 27 May 2026

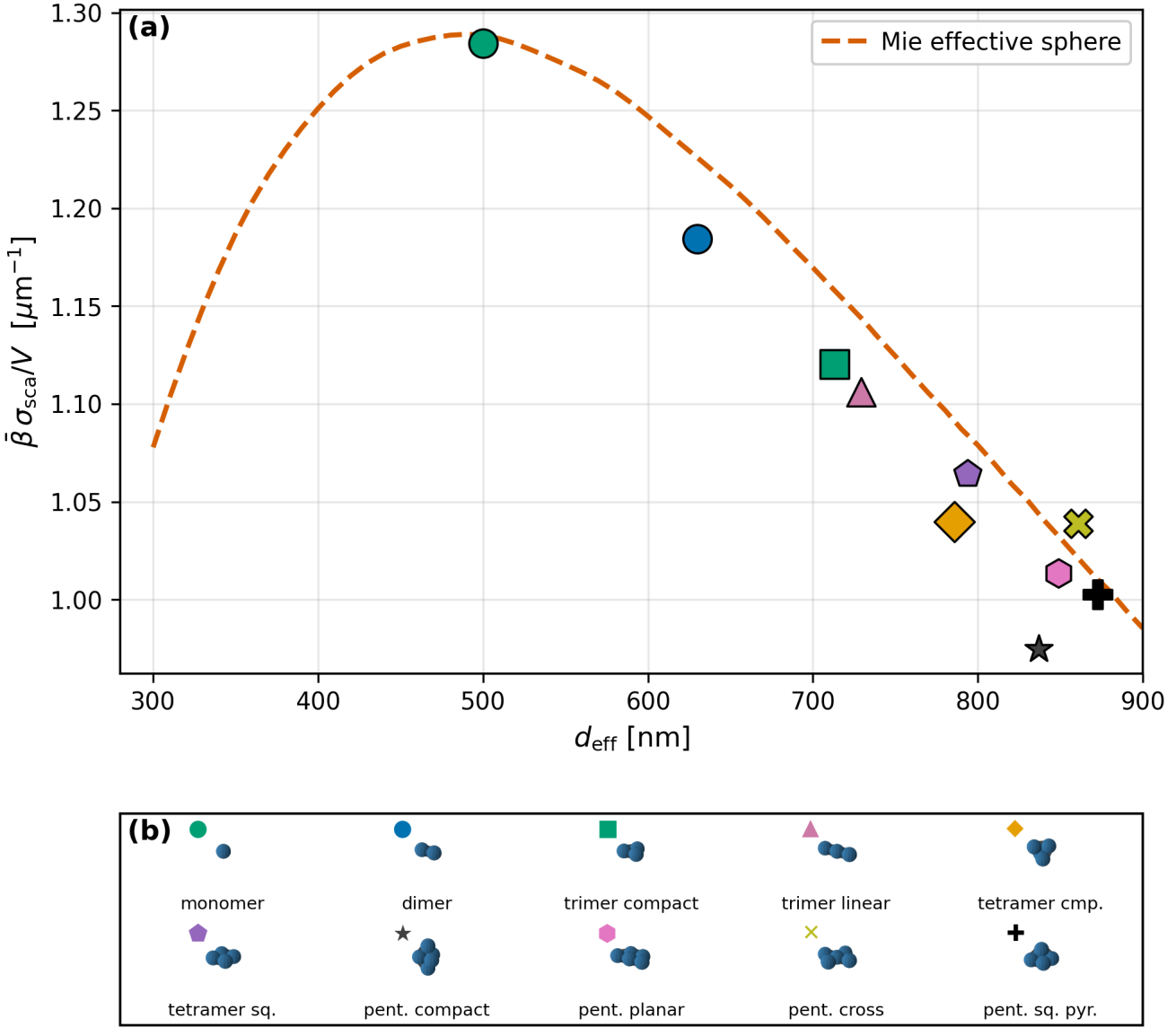

Figure B2. (a) Solar-spectrum-weighted volume-normalized backscatter $\bar{\beta}\sigma_{\mathrm{sca}}/V$ (with $\bar{\beta}$ from Eq. (B11)) versus effective diameter for the SiO_2 monomer and nine aggregate morphologies at monomer radius $R = 250\,\mathrm{nm}$, computed by DDA (symbols) and compared to Mie theory for volume-equivalent spheres (dashed red). (b) Schematic corresponding cluster geometries for panel (a).

Competing interests. The first three authors are affiliated with Stardust Labs Ltd., a sunlight reflection technology development company. Brian E. J. Rose is advising Stardust Labs Ltd.

https://doi.org/10.5194/egusphere-2026-2772
Preprint. Discussion started: 27 May 2026

Acknowledgements. We thank Piers Forster, Dennis Hartmann, Mark Schoeberl, Amyad Spector, and Eli Waxman for useful comments and discussions. We thank Eric L. Fleming for supplying the GSFC 2-D diffusion-coefficient data shown in Fig. A1. Figure 1 is adapted from Chabrillat et al. (2018), with our 2-D model curve and Lagranto trajectory result added on top of the multi-reanalysis comparison originally reported there. The reproduction is made under a Creative Commons Attribution 4.0 license (https://creativecommons.org/licenses/by/4.0/).

https://doi.org/10.5194/egusphere-2026-2772
Preprint. Discussion started: 27 May 2026

References

Andrews, D. G. and McIntyre, M. E.: Planetary waves in horizontal and vertical shear: The generalized Eliassen-Palm relation and the mean zonal acceleration, Journal of the Atmospheric Sciences, 33, 2031–2048, https://doi.org/10.1175/1520-0469(1976)033<2031:PWIHAV>2.0.CO;2, 1976.

Andrews, D. G., Holton, J. R., and Leovy, C. B.: Middle Atmosphere Dynamics, vol. 40 of *International Geophysics Series*, Academic Press, San Diego, CA, https://doi.org/10.1002/qj.49711548612, 1987.

Bala, G., Duffy, P., and Taylor, K.: Impact of geoengineering schemes on the global hydrological cycle, Proceedings of the National Academy of Sciences, 105, 7664–7669, https://doi.org/10.1073/pnas.0711648105, 2008.

Bednarz, E. M., Butler, A. H., Visioni, D., Zhang, Y., Kravitz, B., and MacMartin, D. G.: Injection strategy – a driver of atmospheric circulation and ozone response to stratospheric aerosol geoengineering, Atmospheric Chemistry and Physics, 23, 13 665–13 684, https://doi.org/10.5194/acp-23-13665-2023, 2023a.

Bednarz, E. M., Visioni, D., Kravitz, B., Jones, A., Haywood, J. M., Richter, J., MacMartin, D. G., and Braesicke, P.: Climate response to off-equatorial stratospheric sulfur injections in three Earth system models–Part 2: Stratospheric and free-tropospheric response, Atmospheric Chemistry and Physics, 23, 687–709, https://doi.org/10.5194/acp-23-687-2023, 2023b.

Berk, A., Conforti, P., Kennett, R., Perkins, T., Hawes, F., and van den Bosch, J.: MODTRAN6: a major upgrade of the MODTRAN radiative transfer code, in: Algorithms and Technologies for Multispectral, Hyperspectral, and Ultraspectral Imagery XX, vol. 9088, p. 90880H, SPIE, https://doi.org/10.1117/12.2050433, 2014.

Budyko, M. I.: Climatic Changes, American Geophysical Union, Washington, D.C., https://doi.org/10.1029/SP010, 1977.

Chabrillat, S., Vigouroux, C., Christophe, Y., Engel, A., Errera, Q., Minganti, D., Monge-Sanz, B. M., Segers, A., and Mahieu, E.: Comparison of mean age of air in five reanalyses using the BASCOE transport model, Atmospheric Chemistry and Physics, 18, 14 715–14 735, https://doi.org/10.5194/acp-18-14715-2018, 2018.

Clough, S. A., Shephard, M. W., Mlawer, E. J., Delamere, J., Iacono, M. J., Cady-Pereira, K., Boukabara, S., and Brown, P. D.: Atmospheric radiative transfer modeling: A summary of the AER codes, Journal of Quantitative Spectroscopy and Radiative Transfer, 91, 233–244, https://doi.org/10.1016/j.jqsrt.2004.05.058, 2005.

Coakley, Jr., J. A. and Chylek, P.: The two-stream approximation in radiative transfer: Including the angle of the incident radiation, Journal of Atmospheric Sciences, 32, 409–418, https://doi.org/10.1175/1520-0469(1975)032%3C0409:TTSAIR%3E2.0.CO;2, 1975.

Crutzen, P. J.: Albedo enhancement by stratospheric sulfur injections: A contribution to resolve a policy dilemma?, Climatic Change, 77, 211–220, https://doi.org/10.1007/s10584-006-9101-y, 2006.

Dai, Z., Weisenstein, D. K., and Keith, D. W.: Tailoring meridional and seasonal radiative forcing by sulfate aerosol solar geoengineering, Geophysical Research Letters, 45, 1030–1039, https://doi.org/10.1002/2017GL076472, 2018.

Danabasoglu, G., Lamarque, J.-F., Bacmeister, J., Bailey, D. A., DuVivier, A. K., Edwards, J., Emmons, L. K., Fasullo, J., Garcia, R., Gettelman, A., Hannay, C., Holland, M. M., Large, W. G., Lauritzen, P. H., Lawrence, D. M., Lenaerts, J. T. M., Lindsay, K., Lipscomb, W. H., Mills, M. J., Neale, R., Oleson, K. W., Otto-Bliesner, B., Phillips, A. S., Sacks, W., Tilmes, S., van Kampenhout, L., Vertenstein, M., Bertini, A., Dennis, J., Deser, C., Fischer, C., Fox-Kemper, B., Kay, J. E., Kinnison, D., Kushner, P. J., Larson, V. E., Long, M. C., Mickelson, S., Moore, J. K., Nienhouse, E., Polvani, L., Rasch, P. J., and Strand, W. G.: The Community Earth System Model Version 2 (CESM2), Journal of Advances in Modeling Earth Systems, 12, e2019MS001 916, https://doi.org/https://doi.org/10.1029/2019MS001916, e2019MS001916 2019MS001916, 2020.

https://doi.org/10.5194/egusphere-2026-2772
Preprint. Discussion started: 27 May 2026

Dunkerton, T.: On the mean meridional mass motions of the stratosphere and mesosphere, Journal of the Atmospheric Sciences, 35, 2325–2333, https://doi.org/10.1175/1520-0469(1978)035%3C2325:OTMMMM%3E2.0.CO;2, 1978.

Dykema, J. A., Keith, D. W., and Keutsch, F. N.: Improved aerosol radiative properties as a foundation for solar geoengineering risk assessment, Geophysical Research Letters, 43, 7758–7766, https://doi.org/10.1002/2016GL069258, 2016.

Eastham, S. D. et al.: Key gaps in models' physical representation of climate intervention and its impacts, Journal of Advances in Modeling Earth Systems, 17, e2024MS004 872, https://doi.org/10.1029/2024MS004872, 2025.

Eluszkiewicz, J., Hemler, R. S., Mahlman, J. D., Bruhwiler, L., and Takacs, L. L.: Sensitivity of age-of-air calculations to the choice of advection scheme, Journal of the atmospheric sciences, 57, 3185–3201, https://doi.org/10.1175/1520-0469(2000)057%3C3185:SOAOAC%3E2.0.CO;2, 2000.

English, J. M., Toon, O. B., and Mills, M. J.: Microphysical simulations of sulfur burdens from stratospheric sulfur geoengineering, Atmospheric Chemistry and Physics, 12, 4775–4793, https://doi.org/10.5194/acp-12-4775-2012, 2012.

Fleming, E. L., Jackman, C. H., Stolarski, R. S., and Considine, D. B.: Simulation of stratospheric tracers using an improved empirically based two-dimensional model transport formulation, Journal of Geophysical Research: Atmospheres, 104, 23 911–23 934, https://doi.org/10.1029/1999JD900332, 1999.

Forster, P., Storelvmo, T., Armour, K., Collins, W., Dufresne, J.-L., Howden, D., Huang, J., Iyogi, S. T., Myhre, G., Mauritsen, K., Naik, V., Stevens, B., Trudinger, P. N., and De Viron, P.: The Earth's Energy Budget, Climate Feedbacks, and Climate Sensitivity, pp. 923–1054, Cambridge University Press, Cambridge, United Kingdom and New York, NY, USA, https://doi.org/10.1017/9781009157896.009, 2021.

Fuglestvedt, J. S., Berntsen, T. K., Godal, O., Sausen, R., Shine, K. P., and Skodvin, T.: Metrics of climate change: Assessing radiative forcing and emission indices, Climatic Change, 58, 267–331, https://doi.org/10.1023/A:1023905326842, 2003.

Gregory, A. and West, V.: The sensitivity of a model's stratospheric tape recorder to the choice of advection scheme, Quarterly Journal of the Royal Meteorological Society, 128, 1827–1846, https://doi.org/10.1256/003590002320603430, 2002.

Hartmann, D. L.: Global Physical Climatology, Elsevier, 2nd edn., https://doi.org/10.1016/C2009-0-00030-0, 2016.

Haynes, P. and Shuckburgh, E.: Effective diffusivity as a diagnostic of atmospheric transport: 1. Stratosphere, Journal of Geophysical Research: Atmospheres, 105, 22 777–22 794, https://doi.org/https://doi.org/10.1029/2000JD900093, 2000.

Heckendorn, P., Weisenstein, D., Fueglistaler, S., Luo, B., Rozanov, E., Schraner, M., Thomason, L., and Peter, T.: The impact of geoengineering aerosols on stratospheric temperature and ozone, Environmental Research Letters, 4, 045 108, https://doi.org/10.1088/1748-9326/4/4/045108, 2009.

Ho, D. J. and Pincus, R.: Two-streams revisited: General equations, exact coefficients, and optimized closures, Journal of Advances in Modeling Earth Systems, 16, e2024MS004 504, https://doi.org/10.1029/2024MS004504, 2024.

Hoffmann, L. and Spang, R.: Reanalysis Tropopause Data Repository, https://doi.org/10.26165/JUELICH-DATA/UBNGI2, 2021.

Holton, J. R.: An advective model for two-dimensional transport of stratospheric trace species, Journal of Geophysical Research: Oceans, 86, 11 989–11 994, https://doi.org/10.1029/JC086IC12P11989, 1981.

Keith, D. W., Weisenstein, D. K., Dykema, J. A., and Keutsch, F. N.: Stratospheric solar geoengineering without ozone loss, Proceedings of the National Academy of Sciences, 113, 14 910–14 914, https://doi.org/10.1073/pnas.1615572113, 2016.

Kitamura, R., Pilon, L., and Jonasz, M.: Optical constants of silica glass from extreme ultraviolet to far infrared at near room temperature, Applied optics, 46, 8118–8133, https://doi.org/10.1364/AO.46.008118, 2007.

https://doi.org/10.5194/egusphere-2026-2772
Preprint. Discussion started: 27 May 2026

Kleinschmitt, C., Boucher, O., and Lohmann, U.: Sensitivity of the radiative forcing by stratospheric sulfur geoengineering to the amount and strategy of the SO_2 injection studied with the LMDZ-S3A model, Atmospheric Chemistry and Physics, 18, 2769–2786, https://doi.org/10.5194/acp-18-2769-2018, 2018.

Leonard, B., Lock, A., and MacVean, M.: The NIRVANA scheme applied to one-dimensional advection, International Journal of Numerical Methods for Heat & Fluid Flow, 5, 341–377, https://doi.org/10.1108/EUM0000000004120, 1995.

Lin, S.-J. and Rood, R. B.: Multidimensional flux-form semi-Lagrangian transport schemes, Monthly Weather Review, 124, 2046–2070, https://doi.org/10.1175/1520-0493(1996)124<2046:MFFSLT>2.0.CO;2, 1996.

Long, L., Querry, M., Bell, R. J., and Alexander, R. W.: Optical properties of calcite and gypsum in crystalline and powdered form in the infrared and far-infrared, Infrared Physics, 34, 191–201, https://doi.org/10.1016/0020-0891(93)90008-U, 1993.

Lostier et al: Uptake of stratospheric species on minerals proposed for stratospheric aerosol injection, draft; preprint forthcoming, 2026.

McIntyre, M. E. and Palmer, T. N.: Breaking planetary waves in the stratosphere, Nature, 305, 593–600, https://doi.org/10.1038/305593a0, 1983.

Mlawer, E. J., Taubman, S. J., Brown, P. D., Iacono, M. J., and Clough, S. A.: Radiative transfer for inhomogeneous atmospheres: RRTM, a validated correlated-k model for the longwave, Journal of Geophysical Research: Atmospheres, 102, 16 663–16 682, https://doi.org/10.1029/97JD00237, 1997.

Modak, A., Bala, G., Cao, L., and Caldeira, K.: Why must a solar forcing be larger than a CO2 forcing to cause the same global mean surface temperature change?, Environmental Research Letters, 11, 044 013, https://doi.org/10.1088/1748-9326/11/4/044013, 2016.

Niemeier, U. and Timmreck, C.: What is the limit of climate engineering by stratospheric injection of SO_2?, Atmospheric Chemistry and Physics, 15, 9129–9141, https://doi.org/10.5194/acp-15-9129-2015, 2015.

Oreopoulos, L., Mlawer, E., Delamere, J., Shippert, T., Cole, J., Fomin, B., Iacono, M., Jin, Z., Li, J., Manners, J., et al.: The continual intercomparison of radiation codes: Results from phase I, Journal of Geophysical Research: Atmospheres, 117, https://doi.org/10.1029/2011JD016821, 2012.

Pitari, G. and Visconti, G.: Two-dimensional tracer transport: Derivation of residual mean circulation and eddy transport tensor from a 3-D model data set, Journal of Geophysical Research: Atmospheres, 90, 8019–8032, https://doi.org/10.1029/JD090iD05p08019, 1985.

Plumb, R. A.: A "tropical pipe" model of stratospheric transport, Journal of Geophysical Research: Atmospheres, 101, 3957–3972, https://doi.org/10.1029/95JD03002, 1996.

Prahl, S.: miepython: Pure Python implementation of Mie scattering, https://github.com/scottprahl/miepython.

Rasch, P. J., Tilmes, S., Turco, R. P., Robock, A., Oman, L., Chen, C.-C., Stenchikov, G. L., and Garcia, R. R.: An overview of geoengineering of climate using stratospheric sulphate aerosols, Philosophical Transactions of the Royal Society A: Mathematical, Physical and Engineering Sciences, 366, 4007–4037, https://doi.org/10.1098/rsta.2008.0131, 2008.

Rose, B. E.: CLIMLAB: a Python toolkit for interactive, process-oriented climate modeling., J. Open Source Softw., 3, 659, https://doi.org/10.21105/joss.00659, 2018.

Rose, B. E. J. and climlab contributors: climlab-rrtmg: A stand-alone Python wrapper for the RRTMG radiation modules, https://github.com/climlab/climlab-rrtmg, python package, companion to the climlab modelling framework, 2024.

Schoeberl, M. R., Jensen, E. J., Pfister, L., Ueyama, R., Wang, T., Selkirk, H., et al.: Water vapor, clouds, and saturation in the tropical tropopause layer, Journal of Geophysical Research: Atmospheres, 124, 3984–4003, https://doi.org/10.1029/2018JD029849, 2019.

Schoeberl, M. R., Toohey, M., Wang, Y., and Ueyama, R.: Stratospheric injection lifetimes, Journal of Geophysical Research: Atmospheres, 130, e2025JD043 928, https://doi.org/10.1029/2025JD043928, 2025.

https://doi.org/10.5194/egusphere-2026-2772
Preprint. Discussion started: 27 May 2026

Seinfeld, J. H. and Pandis, S. N.: Atmospheric Chemistry and Physics: From Air Pollution to Climate Change, John Wiley & Sons, Hoboken, NJ, 3rd edn., 2016.

Soci, C., Hersbach, H., Simmons, A., Poli, P., Bell, B., Berrisford, P., Horányi, A., Muñoz-Sabater, J., Nicolas, J., Radu, R., Schepers, D., Villaume, S., Haimberger, L., Woollen, J., Buontempo, C., and Thépaut, J.-N.: The ERA5 global reanalysis from 1940 to 2022, Quarterly Journal of the Royal Meteorological Society, 150, 4014–4048, https://doi.org/10.1002/qj.4803, 2024.

Spector, A. et al.: Composite sub-micron solid particles engineered to enable safe, controllable, efficient, and practical SAI, in preparation, 2026.

Sprenger, M. and Wernli, H.: The LAGRANTO Lagrangian analysis tool–version 2.0, Geoscientific Model Development, 8, 2569–2586, https://doi.org/10.5194/gmd-8-2569-2015, 2015.

Sun, H., Bourguet, S., Luan, L., and Keith, D.: Stratospheric transport and tropospheric sink of solar geoengineering aerosol: a Lagrangian analysis, npj Climate and Atmospheric Science, 7, 115, https://doi.org/10.1038/s41612-024-00664-8, 2024.

Teller, E., Wood, L., and Hyde, R.: Global Warming and Ice Ages: I. Prospects for Physics-Based Modulation of Global Change, Tech. Rep. UCRL-JC-128715, Lawrence Livermore National Laboratory, https://www.osti.gov/biblio/611779, 1997.

Tilmes, S., Richter, J. H., Kravitz, B., MacMartin, D. G., Mills, M. J., Simpson, I. R., Glanville, A. S., Fasullo, J. T., Phillips, A. S., Lamarque, J.-F., Tribbia, J., Edmonds, J., Vitt, F., and Ghosh, S.: CESM1(WACCM) Stratospheric Aerosol Geoengineering Large Ensemble Project, Bulletin of the American Meteorological Society, 99, 2361–2371, https://doi.org/10.1175/BAMS-D-17-0267.1, 2018.

Vattioni, S., Luo, B., Feinberg, A., Stenke, A., Vockenhuber, C., Weber, R., Dykema, J. A., Krieger, U. K., Ammann, M., Keutsch, F. N., Peter, T., and Chiodo, G.: Chemical impact of stratospheric alumina particle injection for solar radiation modification and related uncertainties, Geophysical Research Letters, 50, e2023GL105 889, https://doi.org/10.1029/2023GL105889, 2023.

Vattioni, S., Weber, R., Feinberg, A., Stenke, A., Dykema, J. A., Luo, B., Kelesidis, G. A., Bruun, C. A., Sukhodolov, T., Keutsch, F. N., Peter, T., and Chiodo, G.: A fully coupled solid-particle microphysics scheme for stratospheric aerosol injections within the aerosol–chemistry–climate model SOCOL-AERv2, Geoscientific Model Development, 17, 7767–7793, https://doi.org/10.5194/gmd-17-7767-2024, 2024.

Vattioni, S., Peter, T., Weber, R., Dykema, J. A., Luo, B., Stenke, A., Feinberg, A., Sukhodolov, T., Keutsch, F. N., Ammann, M., Vockenhuber, C., Döbeli, M., Kelesidis, G. A., and Chiodo, G.: Injecting solid particles into the stratosphere could mitigate global warming but currently entails great uncertainties, Communications Earth & Environment, 6, 132, https://doi.org/10.1038/s43247-025-02038-1, 2025.

Visioni, D., MacMartin, D. G., Kravitz, B., Boucher, O., Jones, A., Lurton, T., Martine, M., Mills, M. J., Nabat, P., Niemeier, U., Séférian, R., and Tilmes, S.: Identifying the sources of uncertainty in climate model simulations of solar radiation modification with the G6sulfur and G6solar Geoengineering Model Intercomparison Project (GeoMIP) simulations, Atmospheric Chemistry and Physics, 21, 10 039–10 063, https://doi.org/10.5194/acp-21-10039-2021, 2021.

Visioni, D., Bednarz, E. M., Lee, W. R., Kravitz, B., Jones, A., Haywood, J. M., and MacMartin, D. G.: Climate response to off-equatorial stratospheric sulfur injections in three Earth system models–Part 1: Experimental protocols and surface changes, Atmospheric Chemistry and Physics, 23, 663–685, https://doi.org/10.5194/acp-23-663-2023, 2023.

Waugh, D. and Hall, T.: Age of stratospheric air: Theory, observations, and models, Reviews of Geophysics, 40, 1–1, https://doi.org/10.1029/2000RG000101, 2002.

Waxman, E., Spector, A., Lederer, Y., Segev, Y., Kislev, T., Yedvab, Y., Kushnir, D., and Yahav, R.: A proposal for the safety and controllability requirements that SRM systems should meet, arXiv preprint arXiv:2604.02283, https://doi.org/10.48550/arXiv.2604.02283, stardust Labs, Ness Ziona, Israel, 2026.

https://doi.org/10.5194/egusphere-2026-2772
Preprint. Discussion started: 27 May 2026

Weisenstein, D. K., Keith, D. W., and Dykema, J. A.: Solar geoengineering using solid aerosol in the stratosphere, Atmospheric Chemistry and Physics, 15, 11 835–11 859, https://doi.org/10.5194/acp-15-11835-2015, 2015.

Welch, R., Cox, S., and Zdunkowski, W.: Calculations of the variability of ice cloud radiative properties at selected solar wavelengths, Applied Optics, 19, 3057–3067, https://doi.org/10.1364/AO.19.003057, 1980.

Wells, A. F., Henry, M., Bednarz, E. M., MacMartin, D. G., Jones, A., Dalvi, M., and Haywood, J. M.: Identifying climate impacts from different stratospheric aerosol injection strategies in UKESM1, Earth's Future, 12, e2023EF004 358, https://doi.org/https://doi.org/10.1029/2023EF004358, 2024.

Western, L. M., Bachman, S. D., Montzka, S. A., and Rigby, M.: MALTA: A zonally averaged global atmospheric transport model for long-lived trace gases, Journal of Advances in Modeling Earth Systems, 16, e2023MS003 909, https://doi.org/10.22541/essoar.168890012.27918585/v1, 2024.

Wiscombe, W. and Grams, G.: The backscattered fraction in two-stream approximations, Journal of the Atmospheric Sciences, 33, 2440–2451, https://doi.org/10.1175/1520-0469(1976)033%3C2440:TBFITS%3E2.0.CO;2, 1976.

Yurkin, M. A. and Hoekstra, A. G.: The discrete dipole approximation: An overview and recent developments, Journal of Quantitative Spectroscopy and Radiative Transfer, 106, 558–589, https://doi.org/10.1016/j.jqsrt.2007.01.034, 2007.

Zhang, Y., MacMartin, D. G., Visioni, D., Bednarz, E. M., and Kravitz, B.: Hemispherically symmetric strategies for stratospheric aerosol injection, Earth System Dynamics, 15, 191–213, https://doi.org/10.5194/esd-15-191-2024, 2024.